



Theses and Dissertations

---

2014-12-01

## Compact Antennas and Arrays for Unmanned Air Systems

James Arthur Eck  
*Brigham Young University - Provo*

Follow this and additional works at: <https://scholarsarchive.byu.edu/etd>



Part of the [Electrical and Computer Engineering Commons](#)

---

### BYU ScholarsArchive Citation

Eck, James Arthur, "Compact Antennas and Arrays for Unmanned Air Systems" (2014). *Theses and Dissertations*. 4297.

<https://scholarsarchive.byu.edu/etd/4297>

This Thesis is brought to you for free and open access by BYU ScholarsArchive. It has been accepted for inclusion in Theses and Dissertations by an authorized administrator of BYU ScholarsArchive. For more information, please contact [scholarsarchive@byu.edu](mailto:scholarsarchive@byu.edu), [ellen\\_amatangelo@byu.edu](mailto:ellen_amatangelo@byu.edu).

Compact Antennas and Arrays for Unmanned Air Systems

James A. Eck

A thesis submitted to the faculty of  
Brigham Young University  
in partial fulfillment of the requirements for the degree of  
Master of Science

Karl F. Warnick, Chair  
Michael A. Jensen  
Richard H. Selfridge

Department of Electrical Engineering  
Brigham Young University  
December 2014

Copyright © 2014 James A. Eck

All Rights Reserved

## ABSTRACT

### Compact Antennas and Arrays for Unmanned Air Systems

James A. Eck

Department of Electrical Engineering, BYU

Master of Science

A simple and novel dual-CP printed antenna is modelled and measured. The patch antenna is small and achieves a low axial ratio without quadrature feeding. The measured pattern shows axial ratio pattern squinting over frequency. Possible methods of improving the individual element are discussed, as well as an array technique for improving the axial ratio bandwidth.

Three endfire printed antenna structures are designed, analyzed, and compared. The comparison includes an analysis of costs of production for the antenna structures in addition to their performance parameters. This analysis concludes that cost of materials primarily reduces the size of antennas for a given gain and bandwidth.

An antenna structure with an annular beam pattern for down-looking navigational radar is proposed. The antenna uses sub-wavelength grating techniques from optics to achieve a highly directive planar reflector which is used as a ground plane for a monopole.

A fan-beam array element is fabricated for use in a digitally steered receive array for obstacle avoidance radar. The steered beam pattern is observed. The element-dependent phase shifts for a homodyned signal in particular are explored as to their impact on beam steering.

Keywords: unmanned air vehicles, unmanned air systems, dual circularly polarized antennas, printed circuit board antennas, planar antennas, digital beam steering, antenna arrays, sub-wavelength grating, electromagnetic orientation, sense-and-avoid radar

## ACKNOWLEDGMENTS

I would like to thank my wife, Nichole, and daughter, Sage, for their loving patience in supporting me as I researched and wrote this thesis.

I would also like to thank Dr. Warnick for his wisdom and guidance with regards to this thesis and my graduate studies. He, and my other professors, have broadened my knowledge of electromagnetics and, more fundamentally, taught me to think critically and analytically.

I would also like to recognize my father, Arthur Eck, who first inspired my interest in electrical engineering at a young age and has encouraged me in this work.

I have also benefited from the comradery and knowledge of many of my peers, especially Ben Arnold, Richard Black, James Mackie, Matt Morin, Jonathan Spencer, and Zhenchao Yang.

Thank you to L-3 Communications for the use of their antenna pattern measurement ranges to measure the patterns of the antennas in this thesis.

Finally, this research was funded and inspired by the the NSF Center for Unmanned Air Systems (C-UAS).

## TABLE OF CONTENTS

<b>LIST OF TABLES</b> . . . . .	<b>vi</b>
<b>LIST OF FIGURES</b> . . . . .	<b>vii</b>
<b>Chapter 1 Introduction</b> . . . . .	<b>1</b>
1.1 Previous Work . . . . .	2
1.2 Contributions . . . . .	4
1.3 Thesis Outline . . . . .	5
<b>Chapter 2 Background</b> . . . . .	<b>7</b>
2.1 Microstrip Patches . . . . .	7
2.2 Antenna Parameters . . . . .	8
2.3 Antenna Arrays . . . . .	10
2.3.1 Adaptive Beam Steering with Phased Arrays . . . . .	10
2.3.2 Summary . . . . .	11
<b>Chapter 3 Two Port Square Patch Antenna with Dual Circular Polarization</b> . . . . .	<b>13</b>
3.1 The Antenna Design . . . . .	14
3.2 Antenna Fabrication . . . . .	18
3.3 Proposed Improvements to the Element . . . . .	21
3.3.1 Kite Patch . . . . .	21
3.3.2 Comb Feed . . . . .	22
3.4 Summary . . . . .	22
<b>Chapter 4 PCB Endfire Antenna Structures for UAS</b> . . . . .	<b>23</b>
4.1 Vivaldi . . . . .	24
4.1.1 Design . . . . .	24
4.1.2 Fabricated Antenna . . . . .	25
4.1.3 Signal Coupling . . . . .	26
4.2 Printed Yagi . . . . .	28
4.2.1 Printed Yagi Parameters . . . . .	29
4.3 Substrate Integrated Waveguide Horn . . . . .	29
4.3.1 SIW Horn Parameters . . . . .	30
4.4 Summary . . . . .	30
<b>Chapter 5 Antenna with Annular Pattern for a Down-Looking Navigational Radar</b> . . . . .	<b>33</b>
5.1 Annular Antenna Beam Pattern to Achieve Consistent Reflection Over a Wide Region . . . . .	34
5.1.1 Solution using Metal Reflector Cone . . . . .	34
5.1.2 Sub-Wavelength Grating Reflector Solution . . . . .	35
5.2 The Fabricated Antenna . . . . .	36
5.3 Electromagnetic Orientation . . . . .	37
5.4 Summary . . . . .	39

<b>Chapter 6</b>	<b>Digital Beam Forming for a Search and Track Radar</b>	<b>41</b>
6.1	4x1 Vivaldi Array	42
6.2	4x4 Vivaldi Array with Azimuthal Beam Steering	45
6.2.1	Beam Steering	46
6.3	Broadband Beam Steering	49
6.3.1	Carrier Frequency Phase Shift	53
6.3.2	Homodyne Chirp Dispersion	54
6.3.3	Beat Frequency Beam Squinting	56
6.3.4	Large Array Phase Contribution	56
6.4	Summary	57
<b>Chapter 7</b>	<b>Conclusion</b>	<b>59</b>
7.1	Future Work	59
<b>REFERENCES</b>		<b>61</b>

## LIST OF TABLES

4.1 Endfire Antenna Comparisons . . . . .	31
---	----

## LIST OF FIGURES

3.1	HFSS model of the dual CP antenna. A square patch with chamfered corners produces circularly polarized signals when fed with a split feed. . . . .	14
3.2	Simulated S-parameters of the dual-circular polarization antenna demonstrate good matching, but reveal significant coupling. . . . .	15
3.3	Simulated gain pattern for both the co and cross polarizations. While the intended polarization is high over a broad angular range, the cross polarization is low only over a narrow angular range. . . . .	16
3.4	Isolation between the desired polarization and the undesired polarization is over 20 dB over a 10° angular range. . . . .	17
3.5	Fabricated antenna closeup. Despite its small size, the antenna’s features can be accurately fabricated using standard etching techniques. . . . .	18
3.6	Measured S-Parameters for the CP antenna. These demonstrate a similar frequency response as seen in simulation. The bandwidth is greater when fabricated, from 17 GHz to 22.5 GHz. There is also less coupling, though it is still higher than desired. . . . .	19
3.7	The boresight axial ratio of the antenna by frequency. The axial ratio of the antenna at boresight is not very high quality, but full axial ratio pattern measurement demonstrate that the antenna has high quality CP over angular ranges off boresight. . . . .	20
3.8	The boresight axial ratio over a smaller bandwidth. Even over the best frequency range for boresight axial ratio, it is unreliable at best. . . . .	21
4.1	Vivaldi element tuned to 10 GHz. It is fabricated using standard etching technology and could be easily mass produced. The antenna is back lit in this picture to show that half of the antenna structure is on the back side. . . . .	24
4.2	Simulated gain pattern for the Vivaldi. The simulated pattern of the Vivaldi antenna predicts a gain of about 7 dB at the 10.25 GHz target center frequency. . . . .	25
4.3	The measured $S_{11}$ of the Vivaldi indicates resonance over a 5 GHz frequency range, including the desired band at 10 GHz. . . . .	26
4.4	The measured gain of the Vivaldi confirms that the realized gain is above 8 dB for the whole desired band from 10 to 10.5 GHz. . . . .	27
4.5	The measured pattern of the Vivaldi antenna has a higher gain than that seen in simulation, but the main lobe is more irregular and narrow. . . . .	27
4.6	The coupling of parallel Vivaldi antennas over spacing at 10 GHz. . . . .	28
5.1	Sub-wavelength grating reflector with monopole. This structure is used to produce a tight annular beam with high gain. . . . .	34
5.2	Gain pattern for the monopole over a reflector ground plane. The antenna produces a tight, annular pattern about boresight in simulation that is optimized for down-looking EO radar. . . . .	35
5.3	Simulated pattern cuts. They indicate over 12 dB of gain at 10° from boresight with sidelobes over 10 dB down at 35° from boresight. The 3-dB width of the annular region is about 10°, from 5° to 15° from boresight. . . . .	36
5.4	The fabricated monopole over SWG ground plane. The antenna was fabricated using an SMA connector soldered to the ground plane and filed to 24 GHz resonance. . . . .	37

5.5	Measured pattern overlaid with simulated pattern. The fabricated antenna has a measured pattern that, when normalized, aligns well with the simulated pattern. . . . .	38
5.6	Simulated norm of the difference between a measured channel matrix at a reference position and a mapping of channel matrices. The norm of the difference is significantly lower when compared to map matrices for points near the reference position, allowing us to predict the UAV's location based on this minimum. . . . .	39
6.1	4x1 Vivaldi array. This fixed-feed, four-Vivaldi-element array achieves a fan beam at endfire from the board. . . . .	42
6.2	Measured return loss for the Vivaldi array. It is matched from 8.5 GHz to 12.2 GHz.	43
6.3	The measured gain of the Vivaldi array. It is much cleaner than the pattern seen in measurements of the single Vivaldi. . . . .	43
6.4	The measured gain of the antenna over frequency. It is more than 12 dB, a significant gain over the single Vivaldi. . . . .	44
6.5	A heat map plot of the Vivaldi array's full measured gain pattern. This confirms that the pattern behaves regularly outside of the beam cuts in Figure 6.3. . . . .	45
6.6	A plane wave incident to a two-element array at the angle $\theta$ , propagating in the $\vec{S}$ direction. . . . .	46
6.7	Nine simulated beams for the 4x4 array. At extreme steering angles, strong side lobes are seen. . . . .	47
6.8	Simulated peak gain over steering angle for a narrow band signal. The 4x4 array has an additional 6 dB of gain forward looking and a 3-dB steering range of 90° in simulation. . . . .	48
6.9	The narrow band, simulated side lobe levels for the array, representing the gain of the main lobe minus the largest side lobe's gain at a given steering angle. They are more than 8 dB over the full 90° steering range. This means that a target at a given range and angle will appear over four times as bright as its image at steering angles where it is in a side lobe. . . . .	49
6.10	The narrow band, simulated 3-dB beam width of the steered beam. This beam width determines how wide targets appear to the radar because as the beam is steered the target remains in the beam over a steering range equal to the beam width. Targets at the edges of the steering range will appear wider than those directly in front of the UAV. . . . .	50
6.11	The simulated radar image for four targets. Note that each target has weaker 'ghost images' where it appeared in the side lobe of the steered beam, especially near the edge of the angular steering range. . . . .	51
6.12	This is a radar image like that in Figure 6.11, except that the homodyning dispersion and other broadband effects discussed in Section 6.3 are present in the simulation. The noise level is higher and side lobes are stronger relative to the main lobe. Side lobes also appear to have become more frequent and some targets are indiscernible from their 'ghost images' in sidelobes. . . . .	55

## CHAPTER 1. INTRODUCTION

The idea of using unmanned air vehicles (UAVs) for warfare has been explored since as early as 1849, when Austrian bomb balloons were used to replace artillery in attacks on the Italian city of Venice, which could not be approached by traditional artillery on land [1]. Despite mixed results [2], the idea has been revisited and refined since that time. In fact, not only was World War I the first test of airplanes in warfare, but it was also the first attempt at using unmanned winged aircraft as weapons.

One major leap in UAVs from 1849 to 1916 was the use of radio waves to communicate with the UAV. While the Austrian bomb balloons used a long copper wire to trigger their firing mechanism, World War I ‘aerial torpedoes’ were controlled by radio. Electromagnetic understanding had advanced far enough that radio waves were being used for radar and communications. This greatly increased the range, utility, and control of unmanned aircraft over that of the wind guided balloons used by the Austrians. This advancement necessitated the invention of electrically small antennas that could be borne by the UAVs.

The technology continued to improve as applications broadened. During the Cold War, UAVs were used for training targets, reconnaissance, and nuclear testing. These UAVs quickly reached levels of technology capable of Mach 2 to keep pace with combat aircraft of the time. Radio control techniques also continued to improve with mobile control platforms and coordinated flight patterns. In particular, B-17 ‘Flying Fortresses’ were outfitted for unmanned flight to take measurements at nuclear tests from inside the radioactive cloud. They were controlled from a manned B-17 while in flight. The fact that such large aircraft were used is indicative of the size of control systems of the era. As technology improved, the much smaller P-80 ‘Shooting Star’ aircraft was used instead.

Applications for UAVs have continued to broaden as the technology becomes more affordable and compact. In 2013, two unmanned air systems (UAS) were approved for commercial use

in the United States. With applications opening up in package delivery, dam and bridge integrity monitoring, land surveying, event photography, and many more, this industry is growing quickly; antenna technology continues to improve to meet new demands.

Antennas are needed for many purposes in UAS applications. Communications and control systems require antennas for relaying data to and receiving instructions from the ground. They are also an important part of radar systems used for navigation, data acquisition, and collision avoidance.

For truly autonomous flight, the Federal Aviation Administration (FAA) is requiring collision avoidance to have very good coverage and very low failure rate. To meet this requirement, many researchers are developing both optical and radar systems for obstacle detection. Though radars must be larger to provide the same granularity as a camera, they also present many advantages, including accurate ranging, reduced processing, and cloud penetration. In order to harness these advantages in a limited payload, the radar systems must be made smaller and this includes reducing the size of antennas used in the system.

In this thesis, I discuss a number of lightweight, compact PCB antennas for communications and radar on UAS. Affordability is a major concern for commercial products and additional payload capacity is expensive for UAS. For this reason, commercial UAS require low-cost, compact, and lightweight antennas and other systems.

## **1.1 Previous Work**

With the market for unmanned air systems growing rapidly, UAS have become a hot research topic in many technical fields including mechanical engineering, electrical system design, and antenna design. As aircraft become smaller, antenna researchers have focused much of their effort on shrinking antennas designed for systems on those aircraft. Researchers have also endeavored to integrate antennas on small aircraft without impacting their aerodynamics.

One approach to the problem has been to use printed circuit board (PCB) antennas, which are light-weight, planar, compact, and inexpensive. They also have an inherently high aperture efficiency and therefore translate board area to directivity at a high rate of return. These antennas also rely heavily on high frequencies to be electrically large for a small physical size. This small physical size is also a benefit to the size of systems using the antenna, shrinking processing boards.

Increasingly precise fabrication technology makes arrays of patches feasible at X-band [3], K-band [4], and even higher up to Y-band [5].

Another popular approach has been to create a multipurpose antenna which, though physically large, can serve multiple systems and so reduce the total payload. These antennas must be wide-band and omni-directional in order to serve their purpose. Printed dipoles and traditional dipoles are often favored under these criteria [6].

One novel solution is to treat the entire UAV as an antenna [7]. Using characteristic modes, this approach can integrate an antenna system with an aircraft that itself is electrically small at the desired wavelength [8]. However, this technique must be applied in its entirety to each UAV chassis, unlike other solutions which can be dropped into any UAV with little modification.

Other ways to integrate an antenna on UAS, apart from using the UAS themselves as antennas, include designing the UAS around an antenna structure [9] and using conformal arrays with powerful signal processing techniques [10]. As with using the body of the aircraft as the antenna, this design approach is not transferable from UAV to UAV.

In some cases, it makes more sense to put systems in a ground station [11]. A ground station with a powerful up-link can communicate great amounts of information to and from the UAV and so use its own systems to complement or replace on-aircraft systems such as sense-and-avoid and navigation. For example, a radar system on the ground can detect the locations of obstacles in the sky and communicate them to the UAV rather than have a radar system on the UAV itself doing the detection.

In this thesis, I present work on high-frequency, printed circuit board antennas for applications in UAS. My research includes antennas used for

- UAV to UAV communication systems,
- UAV to satellite or ground station communication systems,
- UAV sense-and-avoid radar systems,
- and UAV electromagnetic orientation systems.

In communication systems, there is a need for dual circularly polarized antennas. This is an unsolved problem for PCB antennas in the case where the circular polarization is generated by the structure of the antenna itself and not external structures, or ‘native’ dual circular polarization.

Sense-and-avoid radar systems require high gain antennas but a broad field of view. This contradiction of criteria can only be answered with beam steering where a high gain beam is swept over the field of view. This process is well known, but homodyning the signal for use in radar introduces new phase terms that must be accounted for. In homodyning, the transmit chirp is mixed with the receive chirp and range is derived from the resulting frequency tones. This is opposed to a direct sampling radar where the received chirp is mixed with a tone and the processing is much more complex.

For electromagnetic orientation, where the UAV attempts to ascertain its position based on radar channel data for the area immediately below it, a downlooking radar is used. Conventional wisdom is to never look directly downward with a radar due to the overpowering specular reflection that can result from flat surfaces. This direct reflection either drives the radar amplifiers out of their dynamic range or in the best case, if they have adjustable gain, reduce the number of features used for orientation. This application calls for an antenna with an annular radiation pattern, which is a largely unexplored variety of antenna.

## 1.2 Contributions

The following is a list of some of the significant contributions put forward in this thesis:

- A native dual circular polarized patch antenna is presented. Native dual CP patch antennas are sparse in the antenna literature. Those that do exist with high quality circular polarization are multilayer [12] [13], are not truly simultaneous, or are not truly planar [14].
- Three planar, endfire antenna structures are designed, compared, and contrasted on the basis of parameters including bandwidth, radiation pattern, cost, and front-to-back ratio. Planar, endfire antennas are attractive for applications in UAS due to their low profile. Little has been done in the literature to compare endfire antenna structures, especially with respect to cost. This comparison provides a basis for decision making with regards to endfire antenna structures.

- An antenna is designed with a null at boresight for down-looking navigational radar. This antenna is an original design using optical sub-wavelength grating theory to achieve a high-directivity, planar reflector. The reflector is proven as a ground plane for a monopole to produce a directive pattern with a null at boresight. The null at boresight is important for a down-looking radar where specular reflection from directly below can dominate returns and drive the signal out of the dynamic range of amplifiers.
- The phase terms needed for digital beam steering in a homodyne signal radar are derived. While digital beam steering is a well understood technique, homodyning presents new phase terms that degrade the beam. The phase dispersion contributed by homodyning is not directly addressed in the literature [15] [16] [17]. I analyze the element dependent phase terms and calculate the error contributed by each term, with relation to incidence angle and other system parameters.

### **1.3 Thesis Outline**

This thesis is organized as follows:

Chapter 2: Background, discusses the antenna parameters and principles necessary to understand the antenna designs presented herein.

Chapter 3: Dual Circular Polarization Patch, presents a simple patch antenna and feed network for achieving dual circular polarization in a single planar element.

Chapter 4: Endfire Planar Antennas, compares three common antenna designs for endfire radiation patterns. These antennas include Vivaldi, Printed Yagi, and Substrate Integrated Waveguide Horn antennas.

Chapter 5: Antenna with Annular Pattern, presents an antenna with an annular beam pattern and high gain intended for down-looking navigational radar.

Chapter 6: Digital Beam Steering, presents digital array processing for multiple-target tracking radar using an antenna array with fan-beam elements, as well as phase shifting terms introduced by homodyning.

## CHAPTER 2. BACKGROUND

Printed circuit board (PCB) antennas are low profile, lightweight, low cost, and easy to fabricate. These characteristics make them ideal for applications in unmanned air systems (UAS) which have severe payload limits on size and weight.

This chapter explains technical terms [18] [19] and concepts [20] [21] that will be used to describe antennas in this thesis. It presents the well known concepts in antenna theory and array theory that this thesis builds upon.

### 2.1 Microstrip Patches

A patch antenna consists of a conducting layer over a dielectric substrate with a ground plane under the dielectric substrate. This configuration creates a resonant cavity beneath the conducting patch when it is fed either with a probe from below or on one side.

Microstrip antennas radiate due to fringing fields on the edges of the microstrip patch. These fringing fields add in phase at boresight to produce a directive radiated field when the patch is a half wavelength long.

Similarly, a microstrip patch receives an incoming E-field signal when the signal produces a favorable voltage distribution across the patch. This occurs when the incident field arrives at the edges of the microstrip path in phase, i.e. from boresight.

This dependence on voltage phase, together with the reflective ground plane beneath the microstrip patch, results in a directive pattern for a single patch. A microstrip patch produces about 6 dB of pattern gain with a  $60^\circ$ - $90^\circ$  3-dB beamwidth.

## 2.2 Antenna Parameters

Any antenna's performance can be characterized by a handful of functional parameters. These include directivity, radiation efficiency, return loss, polarization, axial ratio, port isolation, and—for arrays—mutual coupling.

The directivity pattern,  $D(\theta, \phi)$ , is an angularly dependent parameter that represents the ratio of the power density radiated by an antenna in a given direction,  $S_{av}(r, \theta, \phi)$ , to the power density radiated by an isotropic radiator with the same radiation power,  $P_{rad}$ :

$$D(\theta, \phi) = \frac{S_{av}(r, \theta, \phi)}{P_{rad}/(4\pi r^2)}. \quad (2.1)$$

Often the maximum value of the directivity pattern is referred to simply as the directivity of the antenna.

Radiation efficiency ( $\eta_{rad}$ ) takes into account the losses of the antenna, primarily due to material losses. It can be expressed as the ratio of the radiated power,  $P_{rad}$ , to the input power,  $P_{in}$ :

$$\eta_{rad} = \frac{P_{rad}}{P_{in}}. \quad (2.2)$$

Radiation efficiency is typically less than 1; a value of 1 indicates a lossless antenna.

The gain pattern of an antenna is the directivity pattern scaled by the radiation efficiency:

$$G(\theta, \phi) = \eta_{rad}D(\theta, \phi). \quad (2.3)$$

The gain pattern takes into account losses in the feeds and the antenna itself. It represents the ratio of the power density radiated by the antenna in a given direction to the power density radiated by an isotropic, lossless radiator with the same input power:

$$G(\theta, \phi) = \frac{S_{av}(r, \theta, \phi)}{P_{in}/(4\pi r^2)}. \quad (2.4)$$

The peak gain of the antenna is often referred to as the gain of the antenna.

Return loss represents the portion of supplied power reflected (rather than transmitted or converted to heat) due to mismatches between the transmission line and the antenna. For a single

port antenna, the return loss can be expressed as the  $S_{11}$ . For multi-port antennas, the return loss on the  $n$ th port (with matched loads on other ports) is represented by the  $S_{nn}$ . It is often defined relative to a characteristic impedance of  $50 \Omega$ .

The polarization of an antenna is vital to its functionality. Any difference in the polarization characteristics between the transmit and receive antennas of a system results in polarization loss of power over the link. The polarization of an antenna is more precisely the polarization of the wave generated by the antenna when excited.

The general expression for a wave's polarization is an elliptical wave defined by its major axis, minor axis, polarization phase difference  $\delta$ , and rotation angle. However, most elliptical polarizations are not particularly useful for communications and radar. Ideal special cases of elliptical polarization, such as linear polarization and circular polarization, are more desirable for communications and radar.

Linear polarization occurs when the axial ratio (the ratio of the major and minor axes) is very large, meaning that the major axis is much larger than the minor axis. Linear polarization in an antenna is easy to achieve with high quality. However, it experiences significant polarization loss if the rotation angle between transmit and receive antennas is different.

Circular polarization occurs when the axial ratio is close to one (0 dB) with a polarization phase difference (the phase difference between vertical and horizontal polarized components) of  $\delta = \pm\pi/2$ . A polarization phase difference of  $\delta = \pi/2$  results in left-hand circular polarization (LHCP), and a polarization phase difference of  $\delta = -\pi/2$  results in right-hand circular polarization (RHCP). Circularly polarized waves do not experience polarization loss due to rotation, but are much harder to produce, often requiring some sort of quadrature hybrid to feed the antenna with two signals  $90^\circ$  out of phase.

Axial ratio indicates the quality of the antenna's polarization. If a linear antenna has a low axial ratio, this means it is losing some power to other polarizations. A circularly polarized antenna with an axial ratio above 0 dB loses some power into the opposite-handed circular polarization.

Channel isolation is a measure of how much one signal bleeds into another for an antenna system that transmits or receives on more than one channel. Ideally, there would be total isolation between the two channels to avoid them interfering with each other. Isolation between channels is achieved by using either different polarizations or wavelengths or both between the channels.

For example, a dual linearly polarized antenna might have one channel that is horizontally polarized and another that is vertically polarized. In this example, the channel isolation will be directly related to the linearity of the two channels.

Conceptually similar to channel isolation is mutual coupling between antennas. Whereas I use the term 'isolation' to refer to the inverse coupling between two ports on the same antenna, I use the term 'mutual coupling' to refer to the coupling of signal from one antenna to another at a given separation distance. Mutual coupling is generally undesirable. For example, in a radar system with separate transmit and receive antennas, mutual coupling between the antennas results directly in noise in the near range bins as the transmit antenna sends some of its power directly into the receive antenna due to mutual coupling. This coupled power is undesirable because it looks like a strong but false target in the radar processing.

## **2.3 Antenna Arrays**

Arrays of antenna elements are often used to obtain higher directivity than can be obtained with a single element. This is achieved by positioning the individual elements such that their signals add in phase in the desired direction. The relative phases of the signals feeding each of the elements can also be used to modify the array pattern. Pattern control (or beam steering) can be done in this way without changing the physical positions of the array elements. Assuming no loss in efficiency from expanded feed networks and phase mismatch, doubling the number of antenna elements in the array should roughly double the directivity.

The array pattern produced by the placement and relative phase of the elements is multiplied by the antenna element radiation pattern to produce the radiation pattern for the array.

### **2.3.1 Adaptive Beam Steering with Phased Arrays**

In a uniform linear array (ULA), a beam can be steered to an angle using progressive phase shifts across the array. On the receive side, this steering can be done in post-processing using digital beam steering to form multiple beam patterns, steer toward the strongest signal, or create nulls in the direction of interfering signals.

On the transmit side, similar measures can be used to steer the beam, but multiple simultaneous beam patterns cannot be formed as in post-processing.

### **2.3.2 Summary**

These terms will form the foundation for the discussion of my antenna designs. Understanding these terms will also shed light on comparisons with other existing antennas. Finally, they will also provide a starting point for my analysis of beam steering complications that arise from a homodyned signal.

### **CHAPTER 3. TWO PORT SQUARE PATCH ANTENNA WITH DUAL CIRCULAR POLARIZATION**

Circularly polarized antennas have a number of advantages in communications. Circularly polarized signals suffer less distortion in the ionosphere than linearly polarized signals. They also negate interference due to multipath [22]. Most importantly for mobile platforms, they do not suffer polarization losses due to rotation in the plane of the antenna. This means that an aircraft communicating with a satellite does not suffer polarization loss as it changes its yaw. Changes in roll and pitch can also be accounted for with a wide pattern or beam steering.

Because right-handed and left-handed circularly polarized signals are orthogonal, antennas can be designed that receive two inputs and transmit two, non-interfering signals simultaneously. This is called dual circular polarization. I will refer to a special class of dual circular polarization as ‘native’ dual circular polarization. The term ‘native’ refers to the fact that the antenna structure itself produces the circular polarization rather than external structures such as quadrature hybrid splitters or phase shifting modules.

Dual CP is often achieved with quadrature hybrid or phase shifting modules, but native dual CP in a planar antenna is an unsolved problem in antenna theory. While solutions on multi-layer PCBs exist with near state-of-the-art performance, high quality dual CP on a single layer board is elusive [23]. Multi-layer boards are expensive and complex to fabricate. While this expense is acceptable for applications with a low fabrication volume (e.g., satellites), in applications with a higher fabrication volume (e.g., RC airplanes) this cost could greatly reduce availability, either because prices are too high or because companies producing them become insolvent. An antenna on a single layer board is lighter and significantly cheaper, so for communication applications on small unmanned air systems (UAS) a single layer antenna is preferred, especially when fabricated in large numbers.

To answer this need, I have developed a novel patch antenna that has high quality, dual circular polarization at 20 GHz in HFSS simulations. Measured results are promising. The fabricated

antenna achieves an axial ratio below 3 dB over a  $10^\circ$  angular range. However, this axial ratio experiences a phenomenon similar to frequency squinting, and the angular range over which the axial ratio is below 3 dB is highly frequency dependent.

### 3.1 The Antenna Design

The initial idea was to use a simple split line that would feed adjacent edges in place of a hybrid quadrature splitter. A patch antenna inherently radiates linear polarized signal when fed in the center of one side. With a square patch with a feed to each adjacent edge, one feed will induce a signal radiating horizontally polarized fields, while the other feed will induce a signal radiating vertically polarized fields. In theory, if these two signals are  $90^\circ$  out of phase and of equal magnitude, then the total radiated field will be circularly polarized. In order to achieve

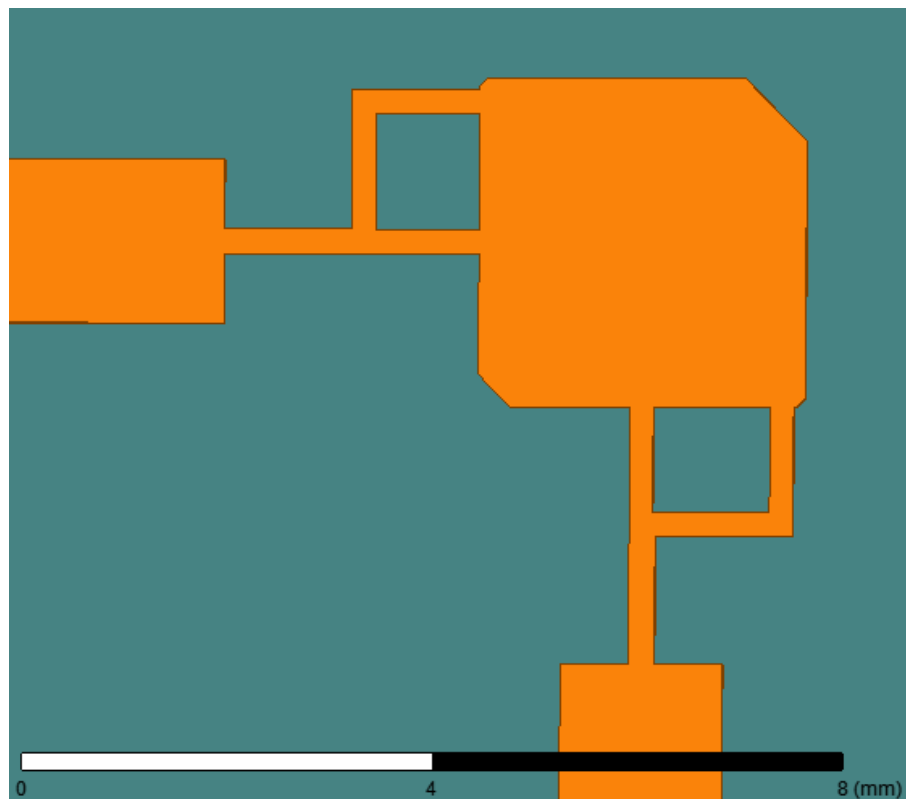


Figure 3.1: HFSS model of the dual CP antenna. A square patch with chamfered corners produces circularly polarized signals when fed with a split feed.

this  $90^\circ$  phase difference, the feed lines to the adjacent edges of the patch need to be different lengths. While one leg of the split line feeds the center of the patch directly, the other leg is given parameterized length and width. The length of the line controls the phase shift between it and the main line. The width of the line governs its impedance and therefore the portion of the signal diverted by the split line. This line was optimized for axial ratio to produce the necessary  $90^\circ$  phase shift using only line length. Over the course of optimization, I discovered that rather than feeding the antenna on two edges, feeding a single edge with one feed at the center and a second feed near the corner produced the best axial ratio performance.

This native dual-CP patch attempts to reproduce the performance of the quadrature feed used in many CP antennas with its simple split-end feed by feeding the antenna at two points on the same side for each handedness of circular polarization. This approach is expected to have less loss than a quadrature feed, approaching the inherent loss of a microstrip line over a dielectric substrate. It also occupies less board area than a quadrature hybrid splitter does.

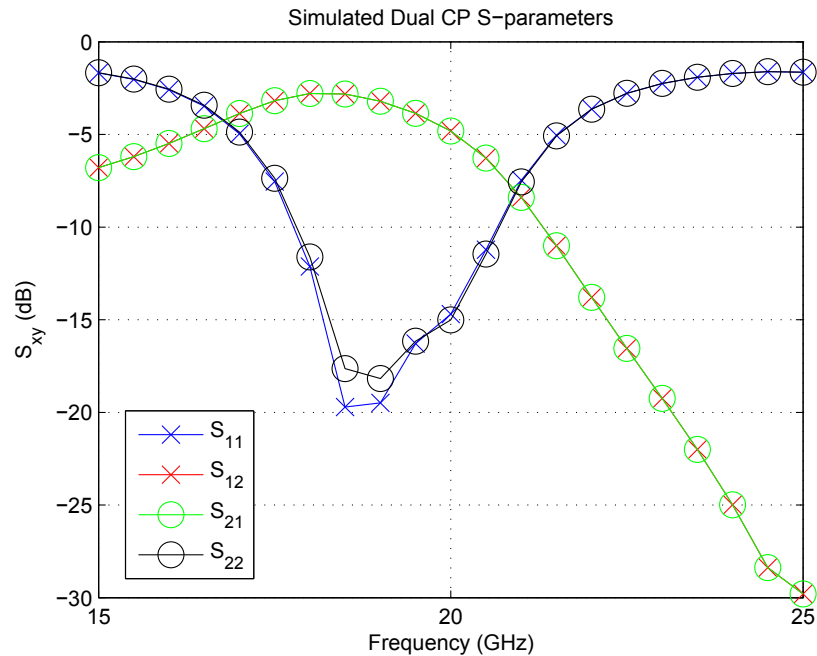


Figure 3.2: Simulated S-parameters of the dual-circular polarization antenna demonstrate good matching, but reveal significant coupling.

Adding a second port with which to feed the orthogonal CP channel interfered with the circular polarization of the initial design, and further optimization was required. I found that chamfering each of the patch's corners provided another degree of freedom that could be used to improve axial ratio. The simulated antenna achieved an axial ratio under 1 dB over an angular range of  $10^\circ$ . Poor isolation was present in simulation. This high coupling,  $|S_{12}|$  over -10 dB, makes the antenna unusable for simultaneous transmit and receive applications. This is because the transmitted signal fed on one port bleeds directly through to the receive signal feed as interference. In general, the transmitted power is significantly greater than the received power and this results in a highly negative SINR. Though in theory this could be calibrated out with a matching network, such a process occupies board space and adds loss. This largely defeats the purpose of removing the quadrature hybrid splitter. A system that switches between transmit and receive modes could also accommodate this coupling, but planar antennas using this method already exist with good performance.

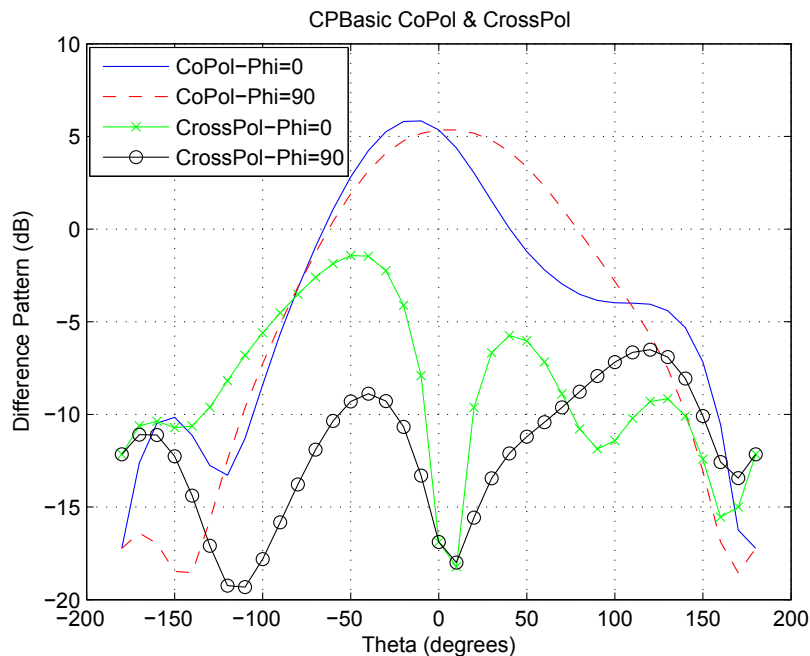


Figure 3.3: Simulated gain pattern for both the co and cross polarizations. While the intended polarization is high over a broad angular range, the cross polarization is low only over a narrow angular range.

Though not so severe as the direct feedthrough in a simultaneous transmit and receive application, a high  $S_{12}$  also degrades the performance of such an antenna when used for dual polarized receive. In this case, the SNR is degraded by a factor related directly to the coupling by the equation

$$T_{rec} = \frac{T_{min}}{1 - |S_{12}|^2}, \quad (3.1)$$

where  $T_{rec}$  is the receive system noise temperature [24]. For this antenna, where the simulated  $S_{12} = -3$  dB in the worst case, this is a 33% increase in the noise temperature.

Similarly, in a dual polarized transmit application, some of the transmitted power will be lost when the signal couples to the other port, leading to a reduction in EIRP of  $|S_{12}|^2$ , or a 25% reduction for this antenna in the worst case.

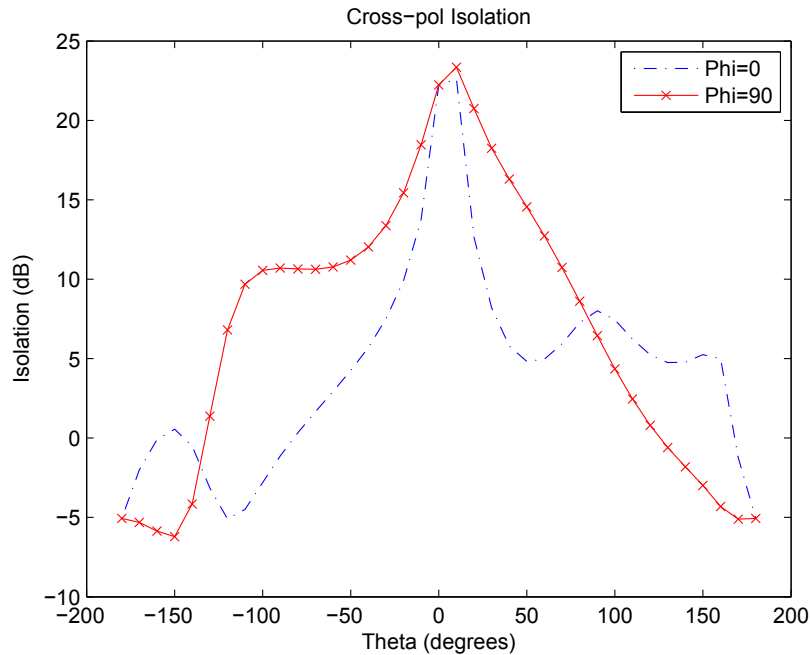


Figure 3.4: Isolation between the desired polarization and the undesired polarization is over 20 dB over a  $10^\circ$  angular range.

### 3.2 Antenna Fabrication

The antenna was fabricated using standard PCB etching techniques, making it very cheap to produce. Due to the antenna's small size (smaller than the body of the connectors used), long feed lines needed to be added in order to prevent interference from the connector body. In simulation, the expansion of the ground plane did not have a significant effect on the antenna performance, so the antenna could instead be integrated in an array or on a board to avoid connector interference and occupy a smaller space on the board per antenna.



Figure 3.5: Fabricated antenna closeup. Despite its small size, the antenna's features can be accurately fabricated using standard etching techniques.

Measurements on a network analyzer were encouraging with the measured S-parameters of the fabricated antenna matching closely those seen in simulation, but with significant improvement. The coupling indicated by  $S_{12}$  was less in measurement than in simulation by about 5 dB, and the return loss was low over a greater bandwidth. This reduces the theoretical increase in receiver noise temperature and reduction in EIRP to only 3%. Based on these favorable S-parameter

measurements, the antenna was expected to conform to simulation in other ways (i.e. pattern and axial ratio).

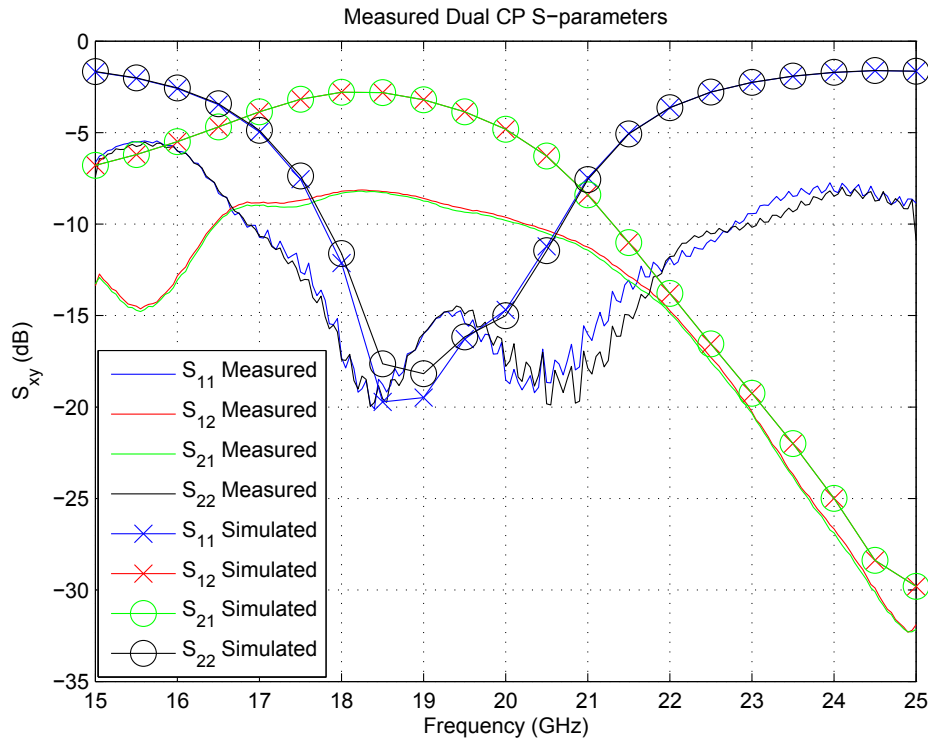


Figure 3.6: Measured S-Parameters for the CP antenna. These demonstrate a similar frequency response as seen in simulation. The bandwidth is greater when fabricated, from 17 GHz to 22.5 GHz. There is also less coupling, though it is still higher than desired.

The fabricated antenna was measured on the L-3 Communication Systems-West large antenna range (Salt Lake City, Utah) to obtain its gain pattern and axial ratio pattern. L-3 Communications has state-of-the-art antenna ranges designed to obtain accurate and consistent measurements. The ranges are climate regulated so the antenna can be measured at a known temperature, and airflow is avoided to prevent motion while taking the measurements. In the large antenna range, the antenna under test is held stationary while a known, well-characterized horn antenna is moved. The test probe is kept in the far field at a distance determined by the wavelength and the size of the antenna under test. The measurement process is lengthy, so the full antenna pattern was

only measured for a few frequencies while the boresight behavior was measured for a larger range of frequencies.

The main beam was very wide, as expected, but the axial ratio pattern was not centered at boresight in measurements. Additionally, the axial ratio pattern exhibited squinting over frequency. While at any given frequency the axial ratio pattern is below 3 dB over various disparate angular ranges, the pattern changes over frequency. Over a frequency of only 0.5 GHz, there is no angular region where the axial ratio is consistently under 3 dB. This severely limits the bandwidth of a communication channel transmitted in a given direction with high quality circular polarization.

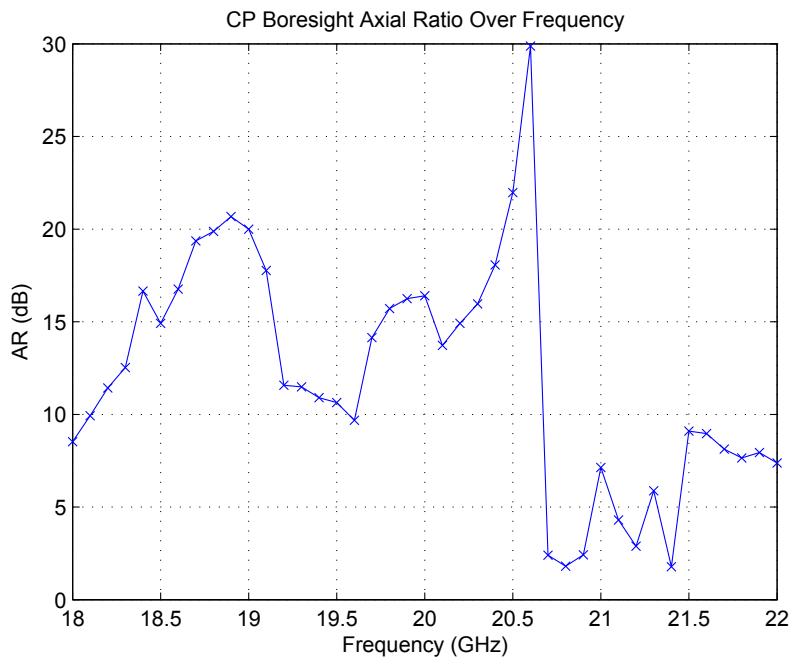


Figure 3.7: The boresight axial ratio of the antenna by frequency. The axial ratio of the antenna at boresight is not very high quality, but full axial ratio pattern measurement demonstrate that the antenna has high quality CP over angular ranges off boresight.

These measurement results suggest that the antenna is not viable as a single element or as a dish feed. Even as part of an array with a beam steered to a particular angular region of low axial ratio, the communication channel would need to be very low bandwidth (e.g. 0.1 GHz). One possibility for improving the axial ratio performance over frequency as part of an array is sequential rotation. This method was first developed 30 years ago and is well understood to improve the

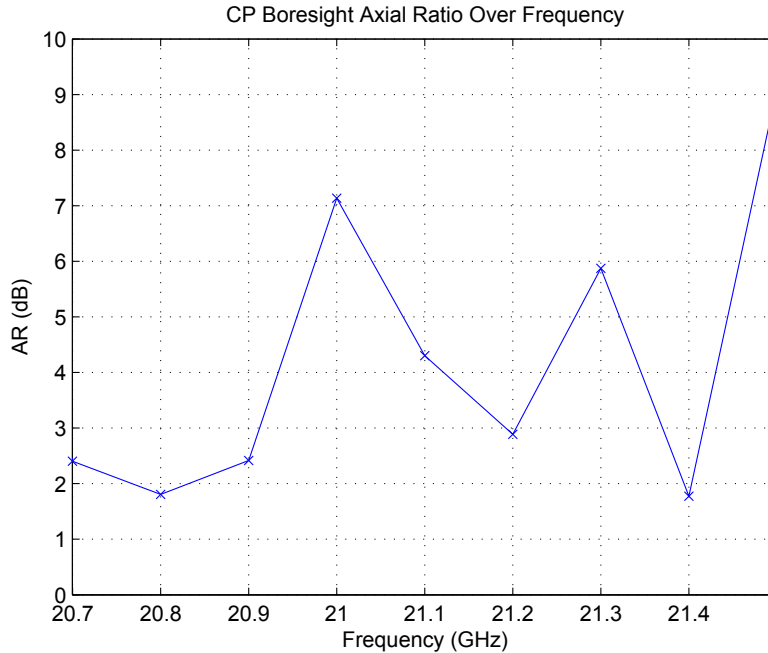


Figure 3.8: The boresight axial ratio over a smaller bandwidth. Even over the best frequency range for boresight axial ratio, it is unreliable at best.

bandwidth of CP arrays [25] [26] [27]. I will discuss other potential options for improving the axial ratio bandwidth of a single element in Section 3.3.

### 3.3 Proposed Improvements to the Element

It is possible that this antenna can be further improved to obtain a better axial ratio bandwidth. I propose two possible changes to the geometry of the antenna: a kite patch shape (rather than square) and an  $n$ -split fan feed. Each of these changes to the structure adds degrees of freedom expected to improve bandwidth after optimization.

#### 3.3.1 Kite Patch

Whatever shape is used for the patch itself must be symmetric about the diagonal line between the two feeds. A square with symmetric chamfers is a simple way to meet this criterion, but a different shape with more optimizable features may be able to achieve an improved axial ratio over bandwidth and angular range. A kite shape is a potential candidate for this optimization. The

slope angle of the kite edges opposite the feed edges adds a degree of freedom. When changed from its current value of  $90^\circ$ , it creates a patch with different electrical lengths across the patch with respect to the two feeds. This requires further exploration to determine its effectiveness in improving the axial ratio bandwidth.

### 3.3.2 Comb Feed

The current design is limited to a two-pronged feed. This means that the phase difference between prongs can change greatly over frequency. By adding one or more additional prongs (whether between or beyond existing prongs) we could add additional parameters of optimization. These prongs would supply additional signal paths that, with optimization, could be made to improve the frequency and angular range over which high-quality CP is transmitted.

## 3.4 Summary

The antenna does face serious challenges in that the axial ratio is below 3 dB only over a narrow beam in the best conditions and there is axial ratio squinting over frequency, which severely hampers its usefulness as a communication antenna. Its channel isolation is also a problem: with higher-than-desired feedthrough from one port to the other ( $S_{12}$ ), the antenna cannot be used simultaneously for receive and transmit. This prevents the antenna from being used in the most common operating mode for dual CP antennas. The poor  $S_{12}$  also reduces the antenna's efficiency as a dual transmit or dual receive antenna, but this reduction is relatively small for the fabricated antenna and the main issue is axial ratio squinting. Sequential rotation could be applied to improve the axial ratio bandwidth of an array of these antennas.

## CHAPTER 4. PCB ENDFIRE ANTENNA STRUCTURES FOR UAS

Open-ended waveguides, horn antennas, and corrugated surface wave structures are traditional and effective ways to design antennas for endfire radiation [28]. While these antenna structures can have high radiation and aperture efficiencies, they are heavy and present a wide profile by the nature of being aperture antennas. For applications in small UAS (unmanned air systems), strict payload restrictions may proscribe the use of these antennas. Printed circuit board (PCB) antennas are light-weight and low-profile and so are preferred for applications in small autonomous aircraft.

Endfire printed antennas such as Vivaldi antennas, Yagi antennas, and substrate integrated waveguide (SIW) horns are useful because of their ability to be built into a board. While this can be achieved to a degree with fixed phase shifts in a patch array, the far extreme of endfire is outside the pattern of a patch. Since a patch antenna only has a 3-dB beam width of about  $90^\circ$ , the half-power steering range of a linear, coplanar array of patches is limited to about  $45^\circ$  in either direction.

Forward-looking sense-and-avoid radar for small UAS is one application for which endfire antennas could be useful. This is because an endfire antenna can achieve a forward-looking beam while still presenting an aerodynamic profile that does not significantly increase the drag of the aircraft. By contrast, a more traditional patch array must be oriented transverse to the direction of flight.

Though the increased drag from the antenna alone may be fairly small, it is also desirable to integrate the antenna with the radar transmit and receive boards. A boresight pattern antenna cannot be integrated without greatly increasing the drag of the aircraft for a board outside a fuselage. Even in a nose cone, small UAS may have a fuselage cross-section too small to contain a radar board positioned transverse to the direction of flight. An endfire antenna, on the other hand, can be integrated with the radar board and keep the radar board aligned with the direction of flight. This orientation can be aerodynamic outside the fuselage or fit into a nosecone on smaller aircraft.

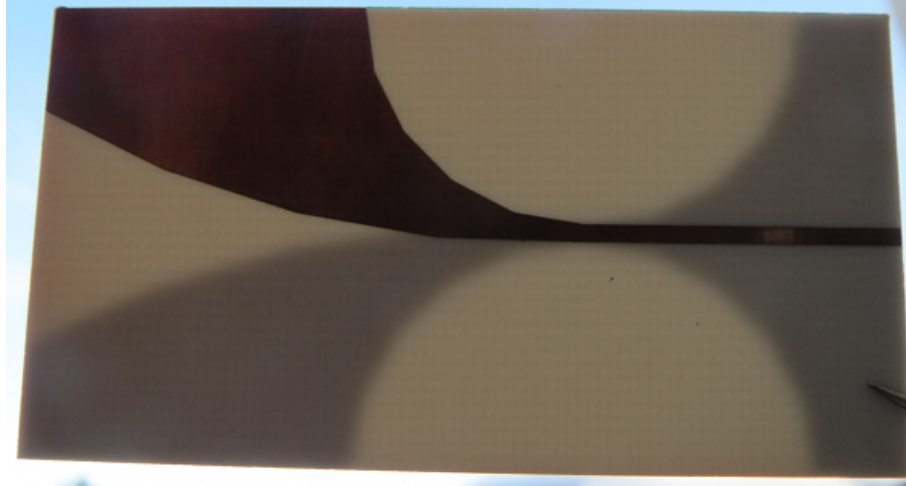


Figure 4.1: Vivaldi element tuned to 10 GHz. It is fabricated using standard etching technology and could be easily mass produced. The antenna is back lit in this picture to show that half of the antenna structure is on the back side.

In this chapter, we will examine three potential endfire antenna structures and compare their performance, size, and cost: the Vivaldi, printed Yagi, and SIW horn. This comparison will explore which design is most effective for translating cost and board real estate into key performance parameters such as gain and bandwidth.

## 4.1 Vivaldi

The Vivaldi antenna, or tapered slot antenna, is favored for its relatively high gain and wide operation bandwidth,  $B/f_c = 30\%$  or so, and a Q-factor of  $Q = 3.33$ . It can be fabricated using standard etching techniques on a single-layer board. This means they can be produced in mass quantities very quickly and very cheaply. For the sake of comparison to other endfire antennas, we have designed and fabricated a Vivaldi antenna at 10 GHz. This Vivaldi is also integrated in an array presented in Chapter 6 for use in a sense-and-avoid radar on the basis of its merits.

### 4.1.1 Design

The Vivaldi antenna was designed in HFSS using geometric shapes, specifically quarter ellipses with circles subtracted. With one such quarter ellipse of copper on each side of the board

and feeds opposite each other, the balun is integrated into the feed [29]. This allows the top fan to be fed at a different polarity than the bottom fan. Optimizing over the two diameters of the ellipses, we achieved the desired center frequency of 10 GHz in simulation with 7 dB gain and a bandwidth of 5 GHz. The front-to-back ratio is 9 dB.

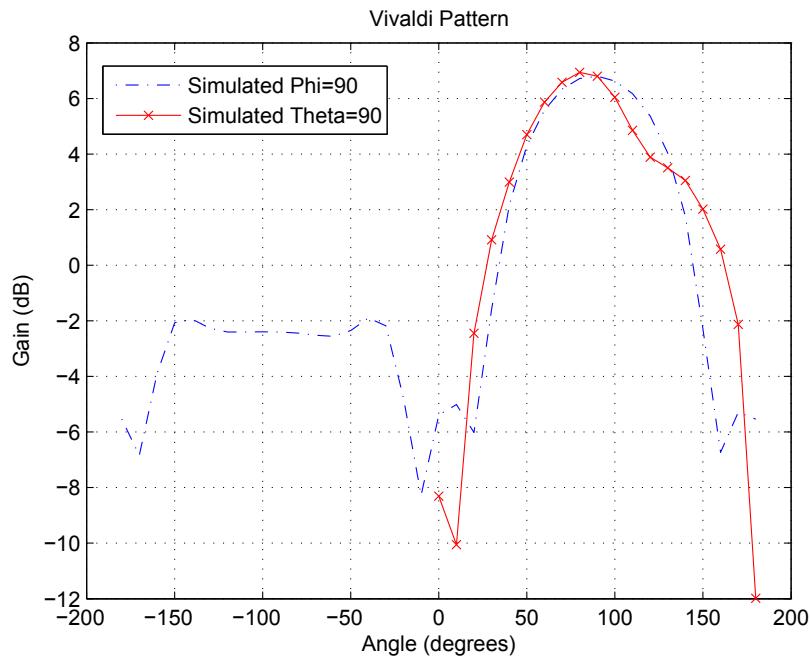


Figure 4.2: Simulated gain pattern for the Vivaldi. The simulated pattern of the Vivaldi antenna predicts a gain of about 7 dB at the 10.25 GHz target center frequency.

#### 4.1.2 Fabricated Antenna

The Vivaldi antenna is fabricated on Rogers 4003C substrate (thickness  $t=0.812$  mm,  $\epsilon_r=3.55$ ). The fabricated Vivaldi achieves a 5 GHz bandwidth in  $S_{11}$  from 9 GHz to 14 GHz, or 43%. This is similar to that seen in simulation. The antenna's gain pattern was measured at the L-3 Communication Systems-West large antenna range (Salt Lake City, Utah). Because the measurement process is very time consuming, this antenna was only measured for its boresight gain over a 0.5 GHz range and azimuthal and elevation pattern cuts were taken at the beam peak. The boresight

gain measurements confirm a consistent boresight gain pattern across the range in question, 10-10.5 GHz, above 8 dB (Figure 4.4). The measured pattern cuts seen in Figure 4.5 show a more irregular pattern than that seen in simulation at 10.25 GHz, possibly due to an extraneous peak off boresight. The peak gain is higher than expected from simulations.

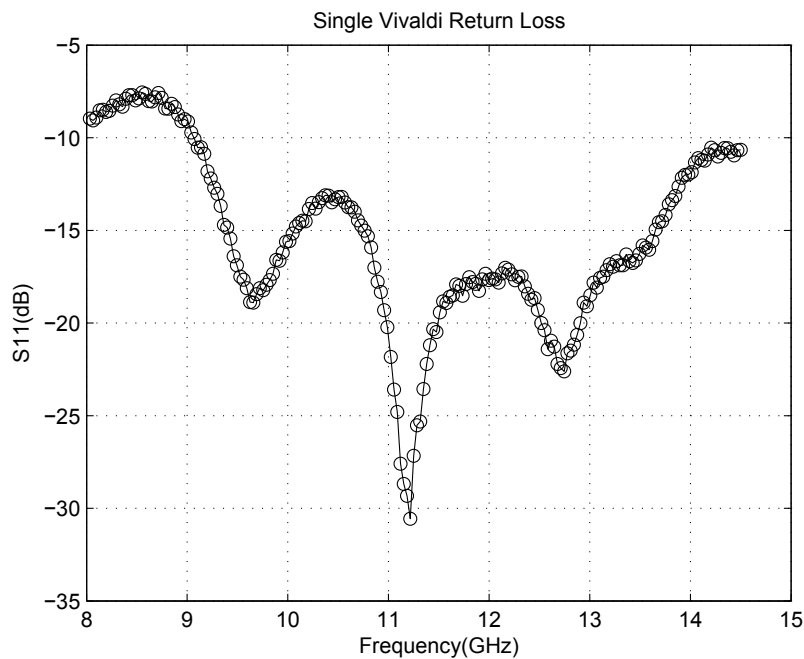


Figure 4.3: The measured  $S_{11}$  of the Vivaldi indicates resonance over a 5 GHz frequency range, including the desired band at 10 GHz.

### 4.1.3 Signal Coupling

Another important antenna parameter for these endfire antennas is the coupling from one antenna port to another. Measurements and simulations agree well for the coupling of the Vivaldi antenna. These measurements, seen in Figure 4.6, indicate coupling of about -50 dB in the best conditions. With the antennas nearer each other, as they would probably be in a radar system, the coupling can be significant at -25 dB when spaced at  $\lambda/2 = 15$  mm in simulation. The highest measured coupling (with 50 mm spacing) was -37 dB, though a closer measurement (with 25 mm spacing) indicated -40 dB coupling, so it is possible the simulation breaks down for small spacing.

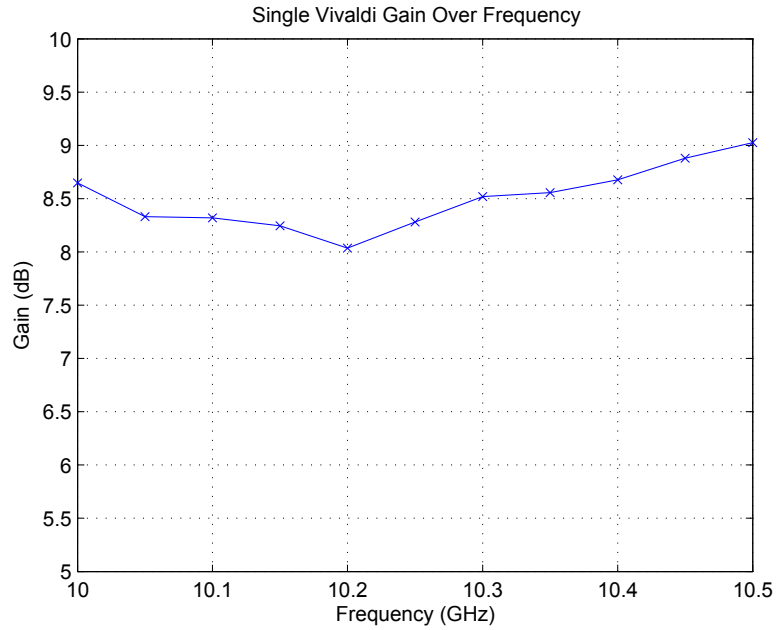


Figure 4.4: The measured gain of the Vivaldi confirms that the realized gain is above 8 dB for the whole desired band from 10 to 10.5 GHz.

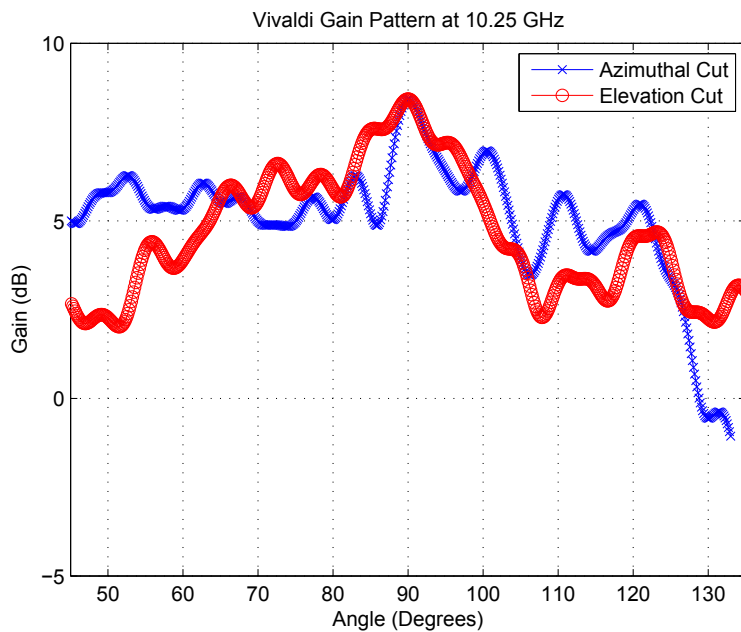


Figure 4.5: The measured pattern of the Vivaldi antenna has a higher gain than that seen in simulation, but the main lobe is more irregular and narrow.

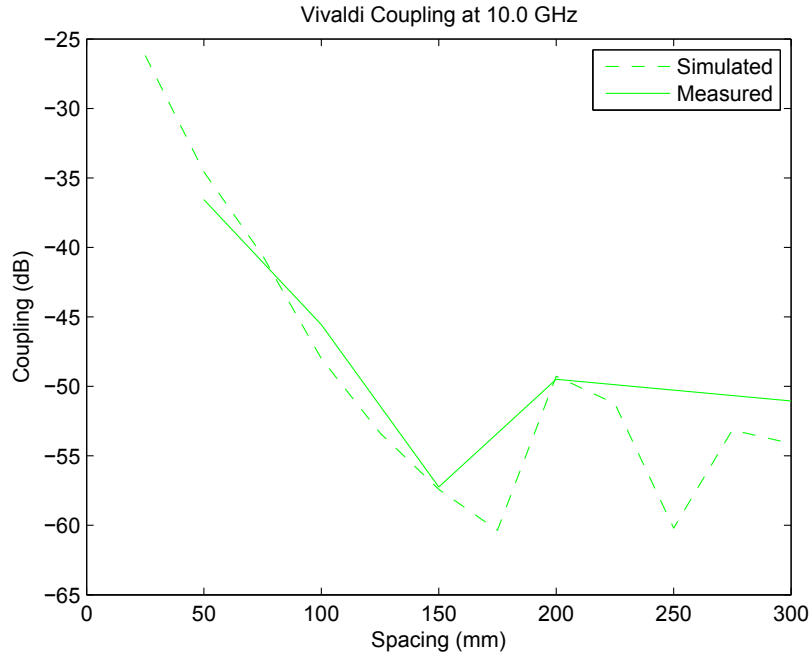


Figure 4.6: The coupling of parallel Vivaldi antennas over spacing at 10 GHz.

With -40 dB of coupling, the Vivaldi element has low enough coupling to prevent a coupled signal propagating from a radar's transmit to its receive from driving the receive amplifiers non-linear. However, even with an ideal coupling value of -60 dB, radar returns from medium-sized targets at a short range are still weaker than the coupled signal. While reducing the coupling is very important for preventing non-linearity in the receive chain, this indicates that the coupled signal will always be stronger than radar returns. The first range bin must always be disregarded because the coupled signal will appear to be a near target if it is not.

## 4.2 Printed Yagi

Another variety of planar, endfire antenna is the printed Yagi antenna. The Yagi-Uda antenna is one of the most well known antennas in the world because it was used for public television reception for decades. Even now, dozens can be seen on rooftops walking around my neighborhood and my father has one in his attic.

The Yagi-Uda antenna is sometimes called a Yagi Array because it consists of a linear array of dipoles. Only one of the dipoles is fed, however, and the other dipoles function either as reflectors or directors for the signal as parasitic elements. The Yagi array can be very directive, depending on the number of directors and reflectors.

A printed Yagi antenna uses the same concept of parasitic reflectors and directors with a printed dipole and printed director and reflector patches. For the sake of this comparison, we use an X-band printed Yagi antenna with two directors designed by M. K. Kan et al. [30]

#### **4.2.1 Printed Yagi Parameters**

The printed Yagi is well matched from 8 GHz to 12 GHz, a 40% bandwidth. It has a peak gain of 7.4 dB at the 10 GHz center frequency, but the pattern is somewhat irregular with sidelobes less than 10 dB down. However, the front-to-back ratio is 15 dB. This is approaching the front-to-back ratio of a traditional Yagi-Uda antenna and very good for a printed antenna.

Like the Vivaldi antenna, the Yagi antenna is printed on single layer board. The antenna dimensions are 19.2 mm x 29 mm on Rogers RT6010 ( $t=0.64$  mm,  $\epsilon_r=10.2$ ).

#### **4.3 Substrate Integrated Waveguide Horn**

A substrate integrated waveguide (SIW), or post-wall waveguide, consists of a waveguide built into a dielectric substrate using the top and bottom copper to form two of the walls of the waveguide and plated vias through the substrate to create the other two walls. These waveguides experience loss due to lossy dielectric, but can also be shrunk significantly due to the high dielectric constant.

An SIW horn antenna uses the same principle as a traditional horn antenna to radiate signal like an open-ended, rectangular waveguide. The high dielectric constant,  $\epsilon_r$ , within the substrate allows us to shrink the waveguide horn's aperture. The fact that the horn is made using standard etching and via techniques on PCB material makes it relatively cheap to produce in large quantities.

For the sake of this comparison, we use a Ku-band horn designed by Marc Esquiús-Morote et al. [31] This horn is designed to push the envelope on wavelengths possible in an SIW horn. Practical constraints of fabricating these antennas tend to preclude their use at frequencies lower

than 20 GHz, but the Esquiús-Morote SIW horn is built for 15 GHz where the substrate thickness must be less than  $\lambda/10$ .

#### 4.3.1 SIW Horn Parameters

The SIW horn is well matched from 14.2 GHz to 16.8 GHz, a 17% bandwidth. It has a peak gain of 8.2 dB at the 15.5 GHz center frequency and the pattern is very regular. The front-to-back ratio is 15 dB, as with the printed Yagi antenna.

This antenna is also printed on single layer board. Its dimensions are  $1.56 \lambda_0 \times 1.26 \lambda_0 \times 0.094 \lambda_0$  on Rogers TMM3 ( $t=1.91$  mm,  $\epsilon_r = 3.27$ ).

#### 4.4 Summary

With the parameters of each of the antennas summarized in Table 4.1, we can compare their performance and cost. The costs are calculated based the size of the antenna, fabrication costs, and a price quote for materials from Rogers Corporation from 29 September 2014. Price ranges are based on bulk pricing from 1-29 panels. With this comparison, we can see how the different antenna structures compare, as well as what benefits are gained from more expensive materials.

The SIW horn is far behind the others with respect to bandwidth, but with a high gain and a highly regular pattern, as well as a good front-to-back ratio, it is still competitive. Its major drawback is in the form of cost. The SIW horn is built on a thick, expensive substrate and while costs reduce dramatically in greater bulk, it is still fairly expensive. Furthermore, the SIW horn is the largest antenna in terms of wavelength; even at its higher frequency it is 50% larger than the printed Yagi and nearly half the size of the Vivaldi. Besides not being a viable approach at the desired 10 GHz band, this significantly higher cost could be prohibitive in mass production, as it is roughly 50% more costly than the printed Yagi and over three times the cost of the Vivaldi.

The printed Yagi has incredible bandwidth and gain within 1 dB of the others, but its sidelobes belie the usefulness of its good front-to-back ratio. It is also the smallest of the three antennas, 33% the size of the Vivaldi and 69% the size of the SIW horn. For an application in UAS, this reduced size is important, and for application in the beam steering radar discussed in

Chapter 6, the wider beam would result in a wider angular steering range than seen with the Vivaldi array. However, the printed Yagi's reduced size is largely due to the high dielectric constant of its substrate. This substrate is significantly more expensive than that used by the Vivaldi antenna and the printed Yagi costs 250% the cost of the Vivaldi, or more depending on material order volume, due to the increased cost of materials.

The Vivaldi antenna has the highest gain and the greatest bandwidth, but it suffers from a worse front-to-back ratio, receiving four times the interfering signal from that direction, and so may not be suitable for a back-to-back application. The Vivaldi is also the largest antenna, more than double the size of the SIW horn and triple the size of the printed Yagi. However, despite the real estate that it occupies on a board, it is significantly cheaper than the other endfire antennas. For systems produced in high volume for applications on small UAVs this price difference could be significant. Particularly for commercial UAS, this difference goes toward reducing the price of the system for the end user and increasing the profit margin for the company.

Table 4.1: Endfire Antenna Comparisons

Parameter	Vivaldi	Printed Yagi	SIW Horn
Peak Gain	8.6 dB	7.4 dB	8.2 dB
Bandwidth	43%	40%	17%
Front-to-Back	9 dB	15 dB	15 dB
Dimensions( $\lambda_0$ )	1.0 x 1.87	0.64 x 0.97	1.56 x 1.26
Cost	\$1.01-1.30	\$2.60-3.29	\$3.38-4.89

## **CHAPTER 5. ANTENNA WITH ANNULAR PATTERN FOR A DOWN-LOOKING NAVIGATIONAL RADAR**

Unmanned air systems (UAS) typically use the global positioning system (GPS) to track their location. While, in general, GPS provides an accurate and dependable service, there are times when it is ineffective. If a UAS is flying through a natural or urban canyon, the UAS likely will not have a line of sight to four GPS satellites, either rendering the UAS partially or completely unable to identify its location. In certain environments, jamming or spoofing can also render GPS ineffective.

To avoid these potential hazards inherent in GPS, a position-recognition radar system can be used in addition to GPS. An electromagnetic orientation (EO) method for GPS-denied navigation based on comparing multiple-input-multiple-output (MIMO) propagation channel responses to stored reference responses has been proposed [32]. Unlike synthetic-aperture radar, for which side-looking antennas are required, the ideal beam orientation for the EO radar is nadir-directed, so that the response measurements are less strongly dependent on UAS orientation. A down-looking antenna with main lobe at nadir would lead to a large specular return, which can drive the radar transceiver electronics nonlinear and contains less position-dependent information about the channel response at a given location than multipath from off-nadir angles.

Accordingly, an antenna with annular pattern and a null in the boresight (nadir) direction is ideal for EO applications. The antenna should also be lightweight, compact and low-profile, to avoid degrading the aerodynamics of the UAS. We first consider a naive design using a monopole and reflector and compare that to a more sophisticated design with a lighter and cheaper sub-wavelength grating (SWG) metasurface planar reflector. This reflector achieves a higher gain and more radially symmetric pattern than the conical reflector. Simulations are used to confirm the performance of the antenna in an EO navigational radar system.

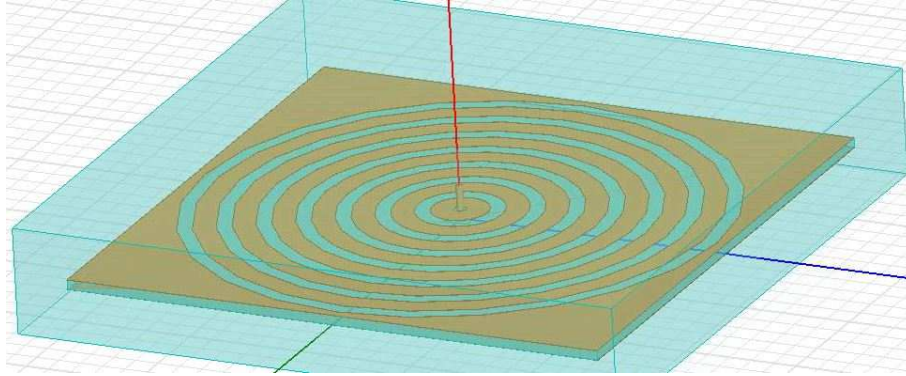


Figure 5.1: Sub-wavelength grating reflector with monopole. This structure is used to produce a tight annular beam with high gain.

## 5.1 Annular Antenna Beam Pattern to Achieve Consistent Reflection Over a Wide Region

In a down-looking radar for navigation, we desire to have a field of view that receives consistent returns for as wide an area as possible in order to maximize the chance of recognizing features. To do this, we require an annular pattern in order to not overemphasize specular returns from directly below the UAS while observing a wide area. We also desire as high a gain as possible to achieve high SNR in the radar return signal from near-nadir incident angles.

### 5.1.1 Solution using Metal Reflector Cone

One way to achieve the desired annular antenna pattern is with a monopole over a ground plane. In order to increase the gain of the antenna and to tighten the beam, we might try placing the monopole in a metal cone to act as a reflector.

In simulation, a monopole tuned to 24 GHz with a cone of radius 15 mm and height 4 mm has a peak gain just under 5 dB, a 3dB center null  $20^\circ$  wide, and an annular beamwidth of about  $40^\circ - 60^\circ$ , depending on the azimuth angle of the cut. While this solution meets many of the needs for an annular antenna, it is heavy and expensive to fabricate. Its gain is also lower and its beam width more variable than would be ideal.

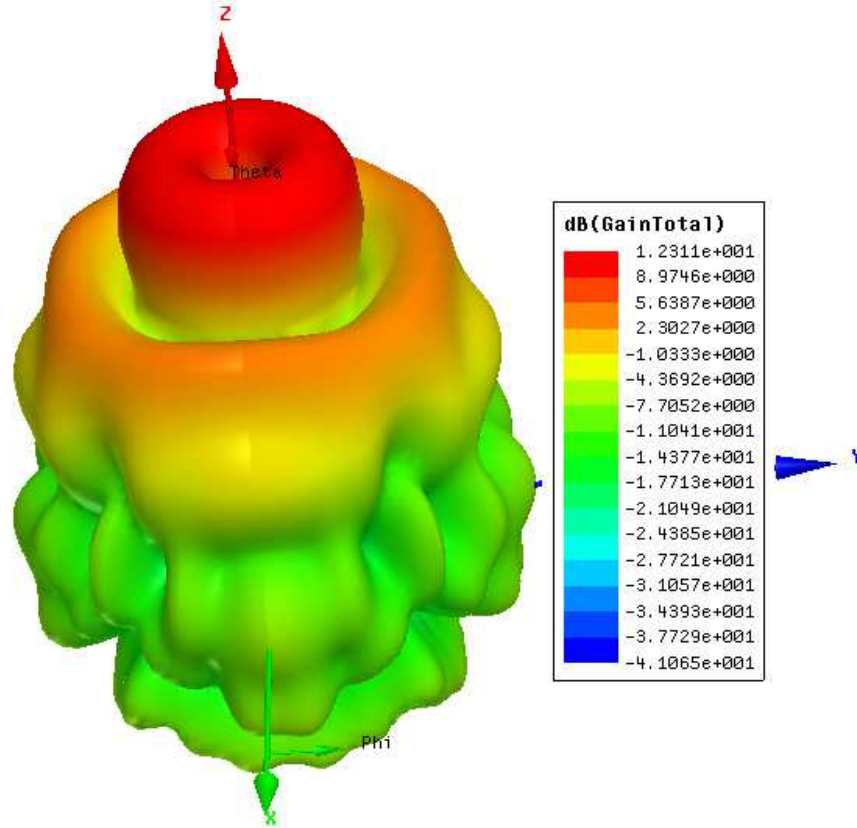


Figure 5.2: Gain pattern for the monopole over a reflector ground plane. The antenna produces a tight, annular pattern about boresight in simulation that is optimized for down-looking EO radar.

### 5.1.2 Sub-Wavelength Grating Reflector Solution

Dielectric gratings have been a well-known technique in optics since the early 1990s [33]. These gratings have been shown to be useful for filters, lenses, and focusing mirrors in optical applications [34]. By scaling these optical results to K-band, we obtain a metasurface ground plane which serves as a focusing reflector for a monopole at 24 GHz.

This monopole with reflector can be seen in Figure 5.1. The gratings have a period of 3.24 mm with a duty cycle of 0.3, about a quarter-wavelength in air. This arrangement avoids the use of a bulky and hard-to-manufacture reflector cone.

The gain pattern of the monopole-over-metasurface ground plane seen in Figure 5.2 and 5.3 demonstrates that the peak gain of the annular pattern is at  $10^\circ$  from boresight all the way around. This  $20^\circ$  null appears to coincide well with a  $10^\circ$  to  $20^\circ$  wide main lobe of monostatic scattering

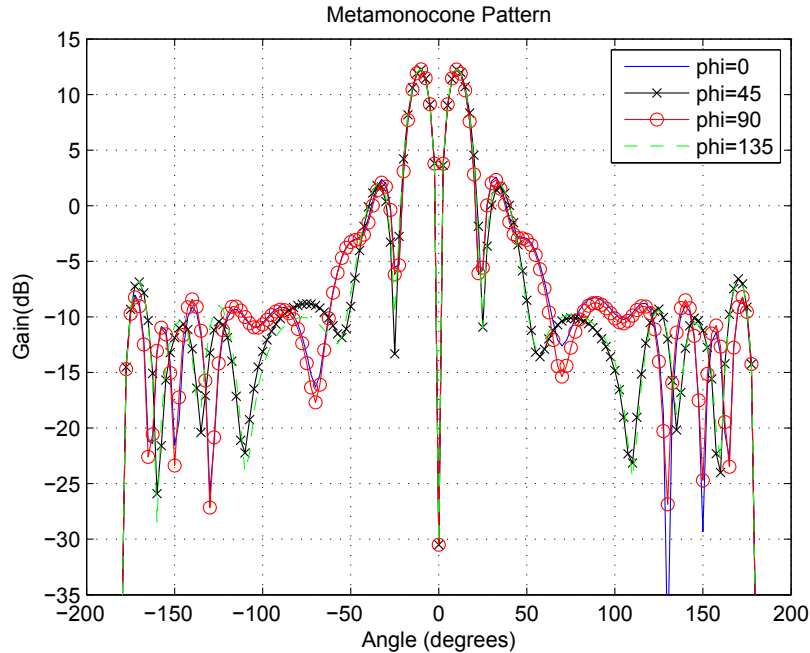


Figure 5.3: Simulated pattern cuts. They indicate over 12 dB of gain at  $10^\circ$  from boresight with sidelobes over 10 dB down at  $35^\circ$  from boresight. The 3-dB width of the annular region is about  $10^\circ$ , from  $5^\circ$  to  $15^\circ$  from boresight.

from a smooth surface [35]. It has a much higher gain than the monopole-in-cone solution at 12.3 dB, and its beamwidth is also more consistent than that of the monopole-in-cone. The SWG reflector is 4 dB larger than the cone reflector, but with 7.5 dB of additional gain, the antenna efficiency is more than double that of the cone. This antenna is also easier to fabricate.

## 5.2 The Fabricated Antenna

The antenna was fabricated using standard etching technology to produce the SWG ground plane. The monopole and feed were achieved by modifying an SMA connector. The monopole is the filed-down pin of the connector itself. This method of fabrication is highly prone to process variation and antenna results were inconsistent. Great care needed to be taken to ensure that the modified SMA connector could be soldered flush with the copper on the back of the etched plane. This preparation guaranteed that the monopole would be exactly vertical, provided it was not bent in the process. Though the process needs refinement and requires great care, the antenna

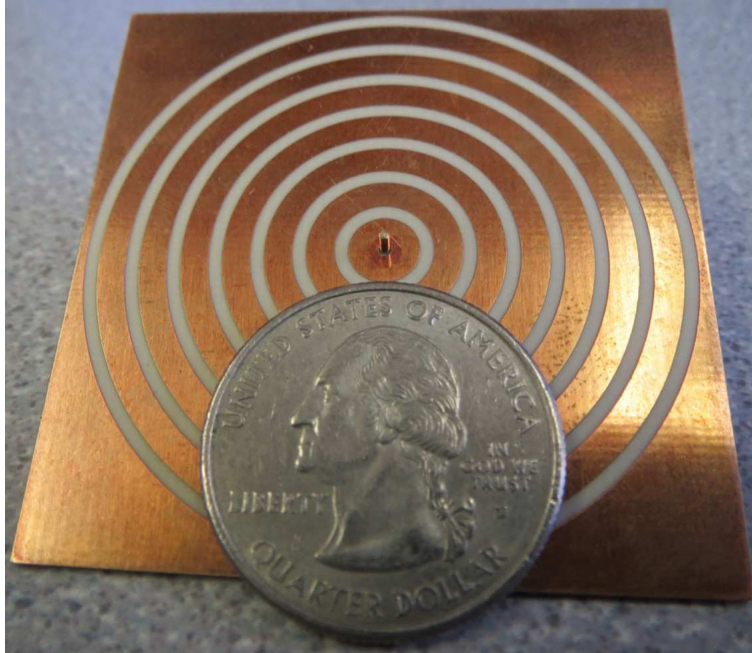


Figure 5.4: The fabricated monopole over SWG ground plane. The antenna was fabricated using an SMA connector soldered to the ground plane and filed to 24 GHz resonance.

shown in Figure 5.4 closely resembles simulation models with a mostly vertical pin-monopole. The connector is flush with the ground plane on the back, which is key to good performance.

The annular pattern performance was measured using a network analyzer, a known patch antenna, and a simple gimbaling mechanism. The distance was kept fixed while the  $S_{12}$  was measured at various mechanically steered angles. As a result of this measurement method, absolute gain values are highly suspect, but the normalized pattern agrees well with the pattern seen in simulation for a linear fit to measured angles, seen in Figure 5.5. Given the crude fabrication and measurement techniques, the pattern agreement is surprisingly good.

### 5.3 Electromagnetic Orientation

The concept of electromagnetic orientation (EO) is to use a down-looking MIMO radar to probe the channel beneath the UAV and produce a channel matrix. This channel matrix is then compared to a map of known channel matrices, ideally from a previous mapping of the region

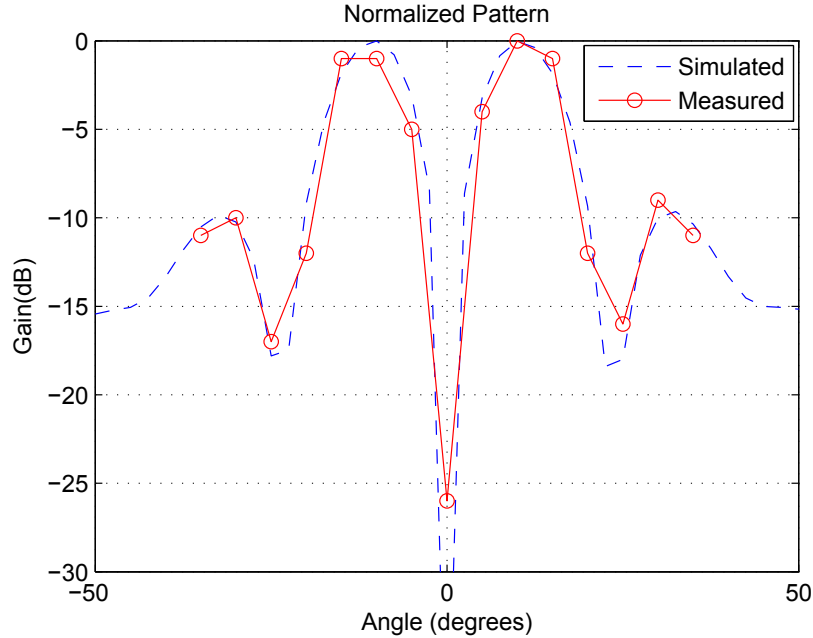


Figure 5.5: Measured pattern overlaid with simulated pattern. The fabricated antenna has a measured pattern that, when normalized, aligns well with the simulated pattern.

using the same radar system. Using this comparison, the UAV can estimate its current position by the location where the norm difference is at a minimum, as proposed in [32] and [36].

To test this method in simulation, we randomly generate a rough surface terrain profile. A path over this terrain is then "mapped" by a simulated four-transmit and four-receive MIMO antenna with annular pattern antennas as array elements. This "mapping" is done by simulating the MIMO channel beneath the UAV at short intervals along the path using a physical optics model for scattering. The channel matrices for each point are saved, comprising the "map" of the path. This mapping is done with an average SNR of 20 dB after introducing electronic and thermal noise.

After completing the "mapping," the MIMO channel is simulated again with an average SNR of 20 dB at a single point along the "mapped" path. Using the method proposed in [32] and [36], the channel matrix obtained from this simulation is compared to each of the "map" channel matrices by taking the norm of the difference of the matrices. The EO system then predicts the location of the UAV to be the global minimum in the norm difference. Data from this simulation in Figure 5.6 indicate that the norm of the difference is at a minimum near the reference location. This implies that using the norm of the difference can accurately estimate the UAV's position.

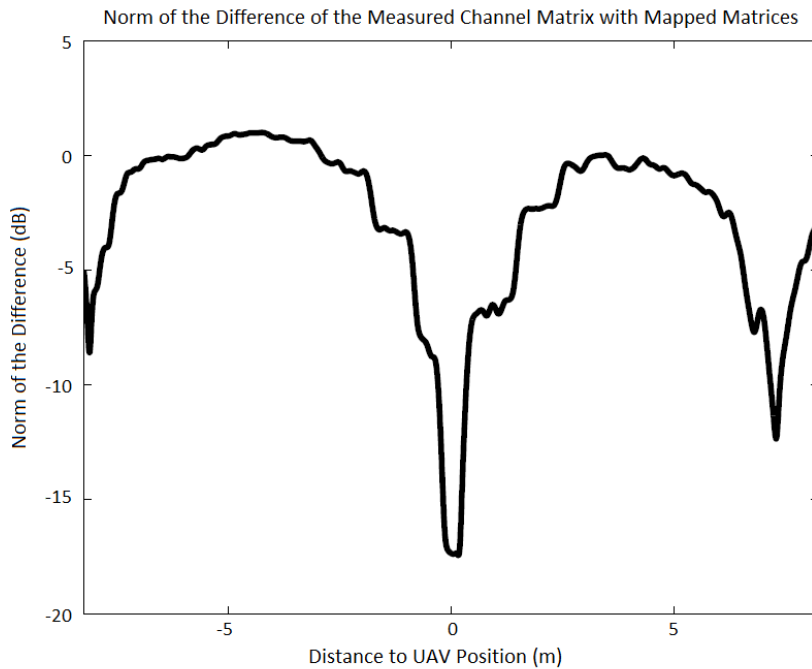


Figure 5.6: Simulated norm of the difference between a measured channel matrix at a reference position and a mapping of channel matrices. The norm of the difference is significantly lower when compared to map matrices for points near the reference position, allowing us to predict the UAV's location based on this minimum.

#### 5.4 Summary

The monopole over sub-wavelength grating reflector antenna achieves a high-gain, annular pattern ideal for preventing specular reflections that normally proscribe the use of a down-looking radar. By applying this as part of an electromagnetic orientation radar, we can obtain channel matrices that take into account features over a broader terrain section for more accurate navigation. This navigation algorithm has been proven in simulation, but requires further testing on a real UAV with a radar system and both normal and annular pattern antennas to verify the improvement in performance from annular antennas.

## CHAPTER 6. DIGITAL BEAM FORMING FOR A SEARCH AND TRACK RADAR

For use in UAS, a BYU research group under the purview of the Center for Unmanned Aircraft Systems (C-UAS) has developed a compact 10 GHz FMCW radar [3]. The purpose of the radar is to detect obstacles and other aircraft and inform an obstacle-avoidance algorithm in order to prevent collisions. This system needs a long range and a wide horizontal field of view, as well as the ability to search for and track targets. Long range (or high gain) and a wide beam are contradictory goals in antenna design, but the criterion to search for and track targets may present a way to marry the two. In order to determine a target's angle-of-arrival information from the radar return, and so track it, a radar with multiple beams is needed. These multiple beams can have a high gain individually, while together comprising a wide field of view. A receive array using digital beam steering best addresses the antenna needs of this system. Such a beam steering radar can produce a radar image through digital processing that maps radar return voltages by both range and angle of arrival.

As seen in the radar equation, one option to increase the range ( $R$ ) of a radar system at a given minimum SNR is to increase the gain of the transmit and receive antennas ( $G_t$  and  $G_r$  respectively):

$$\text{SNR} = \frac{P_t G_t G_r \lambda^2 \sigma}{(4\pi)^3 k_b T_0 B F L_s R^4}. \quad (6.1)$$

This can be done with an array of antenna elements, but has the side effect of reducing the beam width of the antenna. In the case of our forward-looking, sense-and-avoid radar for small UAS, we want a narrow beam in elevation to eliminate ground clutter, which is one of the major limitations for tracking algorithms using radar. However, we also want a broad beam in azimuth to detect targets anywhere in front of the UAV and satisfy regulatory demands for autonomous flight. Both of these conditions can be met with a vertical array of elements. In Section 6.1 we will discuss the characteristics of one such array.

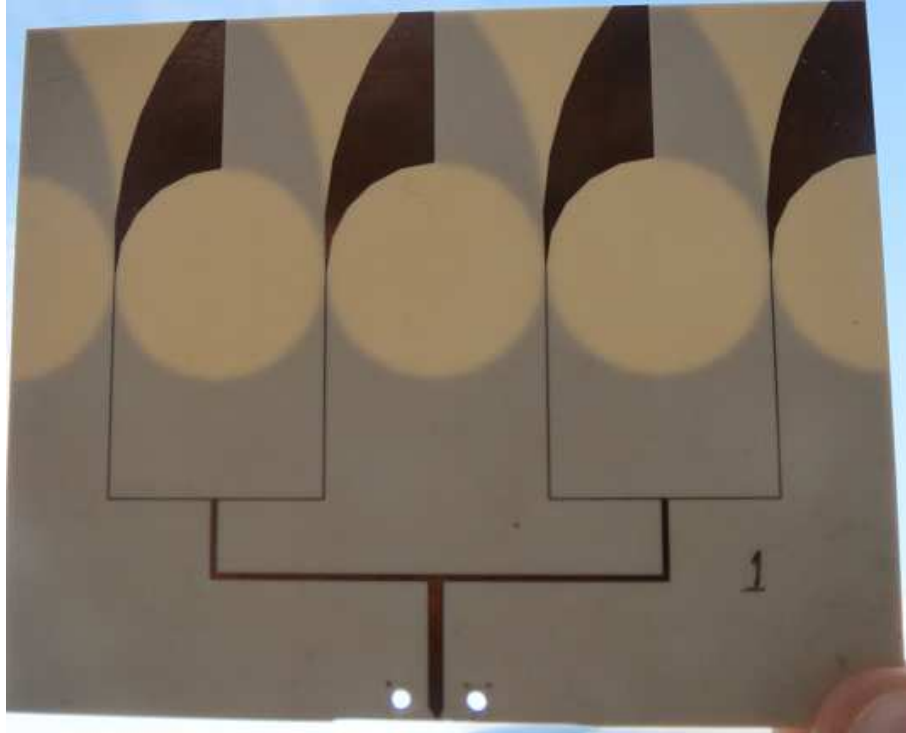


Figure 6.1: 4x1 Vivaldi array. This fixed-feed, four-Vivaldi-element array achieves a fan beam at endfire from the board.

While the wide-look angle in azimuth allows us to detect targets over a broad angular range, it only informs us of the presence and range of the target. We would also like to extract direction or angle of arrival of the target for use in the obstacle-avoidance algorithm. To do this, we propose implementing digital beam steering on the receive chain using independent receive antennas arrayed horizontally. In Section 6.2 we will present an array using digital beam forming and its limitations for detection and tracking.

## 6.1 4x1 Vivaldi Array

As described, our sense-and-avoid radar system requires a narrow vertical beam to eliminate ground clutter. It also requires a wide horizontal beam to provide a wide field of view in front of the aircraft. These two criteria can be met by a vertical array of elements. We prefer an array of endfire elements to more easily integrate with the radar board without affecting the aircraft's drag, as discussed in Chapter 4.

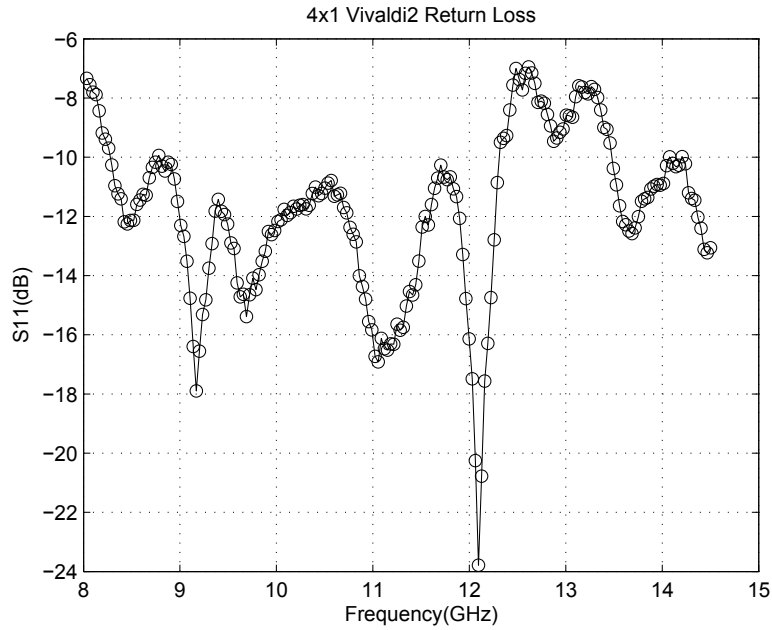


Figure 6.2: Measured return loss for the Vivaldi array. It is matched from 8.5 GHz to 12.2 GHz.

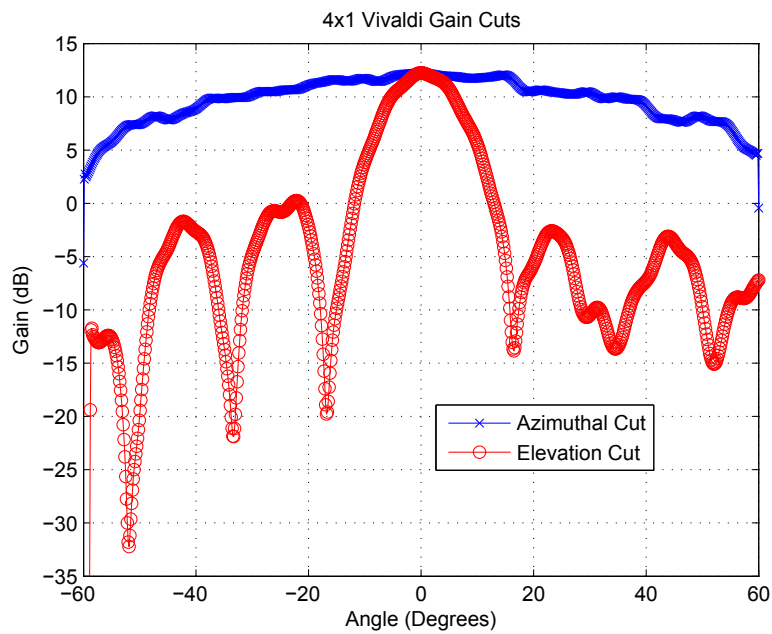


Figure 6.3: The measured gain of the Vivaldi array. It is much cleaner than the pattern seen in measurements of the single Vivaldi.

Using the Vivaldi element presented in Chapter 4 with a simple split-line feed, we produce a passive, fixed-beam array. This array is matched over a frequency band similar to that of the single-element Vivaldi, resonating from 9 GHz to 12 GHz.

This array achieves a fan beam seen in Figure 6.3 with a gain of over 12 dB at endfire. Sidelobes are down 10 dB or more, and in the azimuth cut the pattern is significantly smoother than that seen in the single Vivaldi pattern. As seen in Figure 6.4, the array maintains a high peak gain over the frequency band desired, from 10 to 10.5 GHz, at over 12 dB.

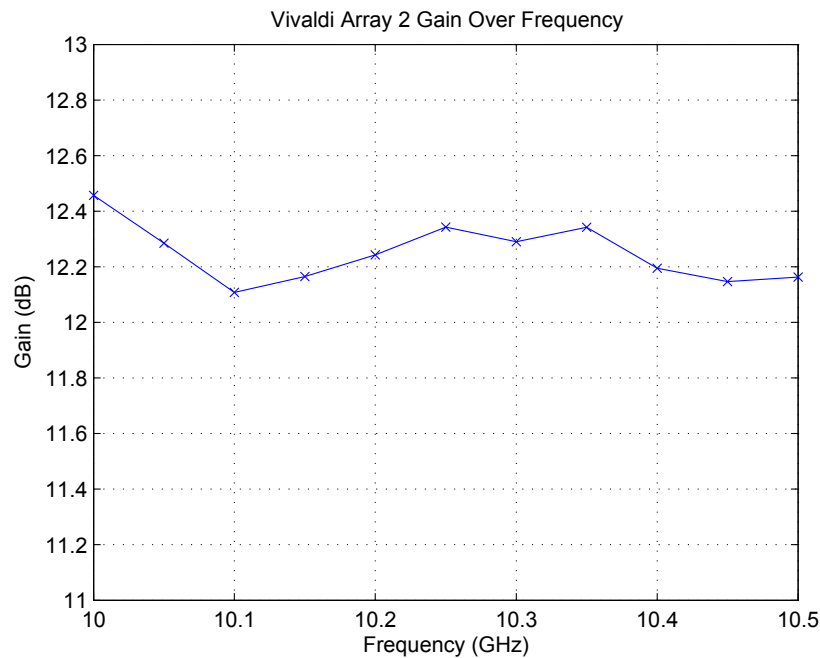


Figure 6.4: The measured gain of the antenna over frequency. It is more than 12 dB, a significant gain over the single Vivaldi.

This fan beam is ideal for our forward-looking, sense-and-avoid radar system. It has wide azimuthal coverage but reduces clutter with a narrow beam in elevation. It also provides a high gain to increase the range of the radar. The antenna itself is lightweight and presents a very narrow profile in the direction of flight.

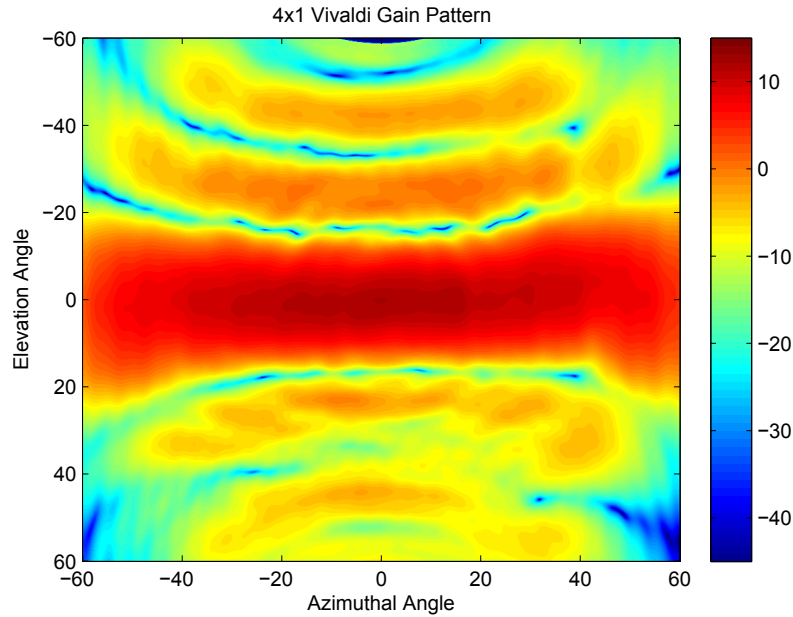


Figure 6.5: A heat map plot of the Vivaldi array’s full measured gain pattern. This confirms that the pattern behaves regularly outside of the beam cuts in Figure 6.3.

## 6.2 4x4 Vivaldi Array with Azimuthal Beam Steering

With the antenna presented in Section 6.1, we achieve a fan beam desirable for our scenario. However, using this antenna alone for transmit and receive in our radar will only provide the algorithm with information about the presence and range of potential obstacles. In this section we will discuss a means of obtaining angle-of-arrival information from the radar signal. This technique will also increase the radar’s range without reducing its field of view.

To obtain angle-of-arrival data from the signal, we will array four of these 4x1 Vivaldi arrays horizontally on the receive channel of the system. The data from each of these channels will be combined using a digital beam forming algorithm to produce a matrix of radar return data indexed by range in one dimension and angle of arrival in the other. With this matrix, we will be able to detect and track multiple targets simultaneously.

## 6.2.1 Beam Steering

Beam steering can be achieved by applying a progressive phase shift to the signals seen on individual antennas. This phase shift corresponds to the angle at which we desire to steer the beam. More precisely, the phase shift needed to steer the beam at a given angle is equal to the phase delay between antennas experienced by an incident plane wave from that angle, as seen in Figure 6.6.

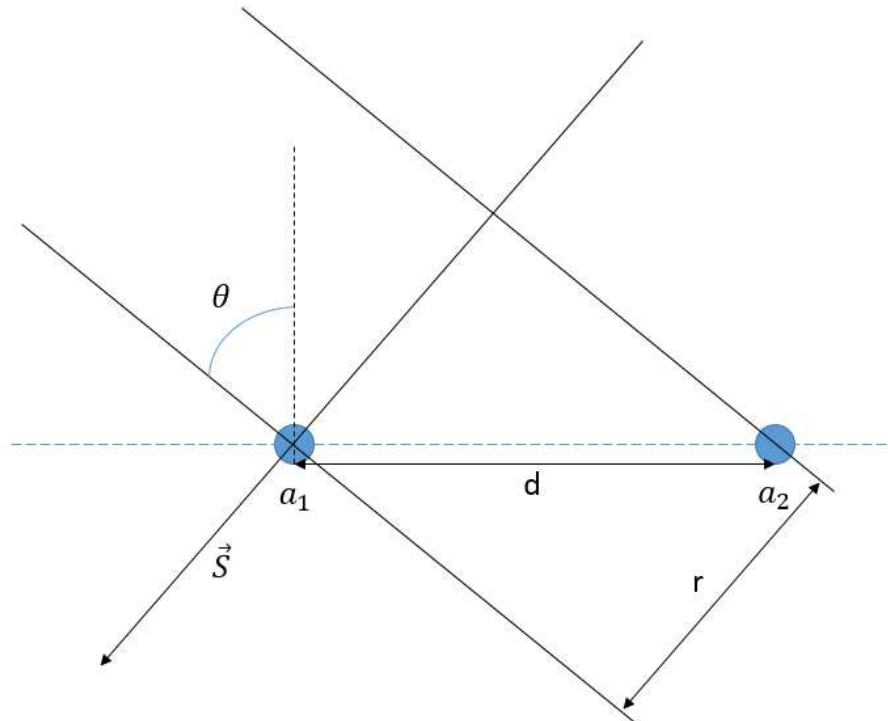


Figure 6.6: A plane wave incident to a two-element array at the angle  $\theta$ , propagating in the  $\vec{S}$  direction.

Based on the depiction of an incident wave in Figure 6.6, we can derive the phase delay ( $\Delta\phi$ ) as a function of steering angle. We begin with  $r = d \cos(\theta)$ , the distance traveled by the incident wave between the time the wave front reaches  $a_2$  and the time it reaches  $a_1$ . This distance is traveled in a time  $\Delta t = r/c_0$  where  $c_0$  is the speed of light in a vacuum. From this we can derive

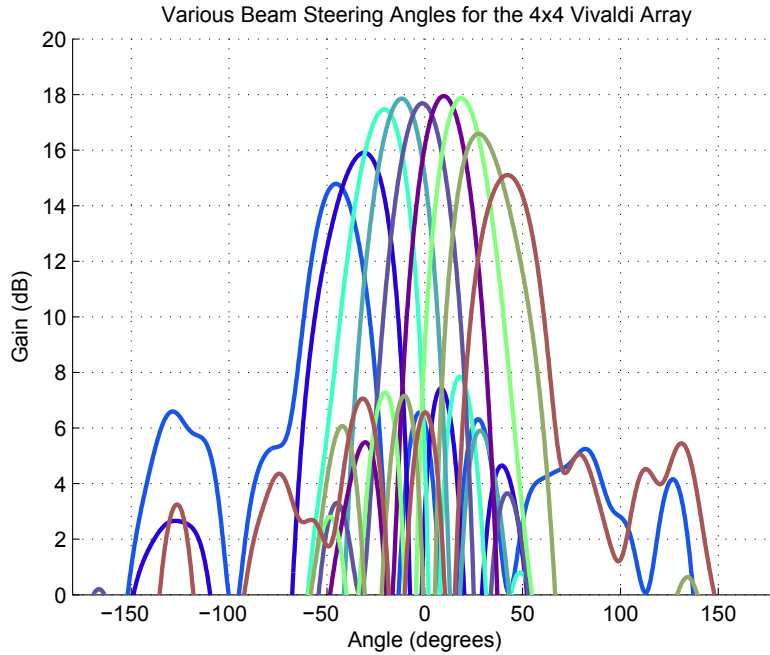


Figure 6.7: Nine simulated beams for the 4x4 array. At extreme steering angles, strong side lobes are seen.

phase delay between  $a_1$  and  $a_2$  to be

$$\Delta\phi = \Delta t\omega \quad (6.2)$$

$$= \frac{\omega d \cos(\theta)}{c_0} \quad (6.3)$$

$$= kd \cos(\theta), \quad (6.4)$$

where  $k = \omega/c_0$  is the spatial frequency, or wave number, of the signal. For a linear array with half wavelength spacing,  $d = \lambda/2$ , at a single tone, we obtain

$$\Delta\phi = \pi \cos(\theta). \quad (6.5)$$

Using this phase shift formulation, we can simulate the ideal receive patterns for various steering angles with our 4x4 array (some examples are shown in Figure 6.7). The peak gain by steering angle as seen in these simulations can be seen in Figure 6.8. The array provides an

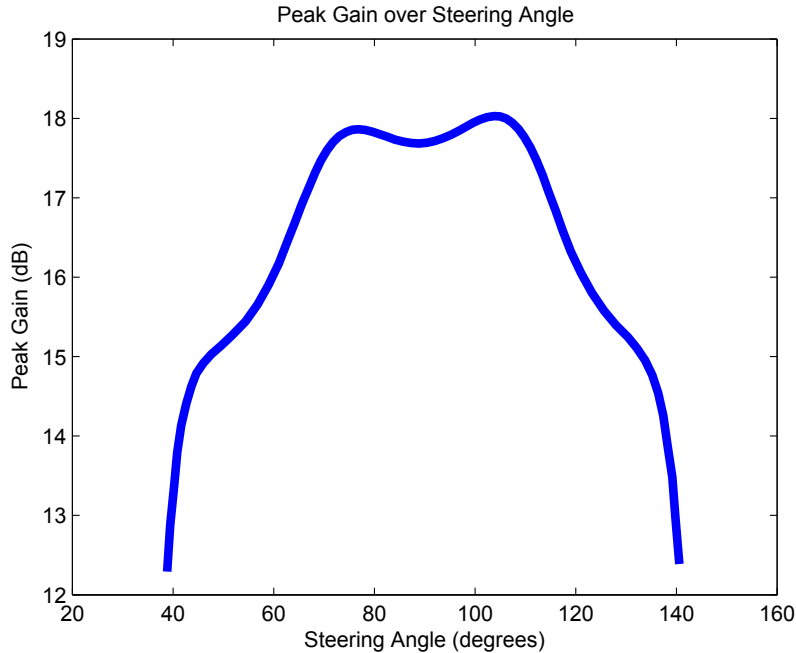


Figure 6.8: Simulated peak gain over steering angle for a narrow band signal. The 4x4 array has an additional 6 dB of gain forward looking and a 3-dB steering range of 90° in simulation.

additional 6 dB of gain at peak with a 3 dB steering range of 90°. The sidelobe levels for the array are above 8 dB over the 90° steering range (Figure 6.9). The beam width of the steered beam is between 25° and 32° for the range (Figure 6.10).

Using these simulated steered beams, we can simulate the function of the radar for multiple targets and produce a "radar image" representing the matrix of return voltages given to the autopilot algorithm after beam steering. This matrix is indexed by the range to the target and the angle of arrival and can be visualized as the "radar image" in Figure 6.11. This visualization sheds light on how bright targets may appear when in the side lobe of a steered beam. Without clever processing, these side lobe images may appear to be additional smaller targets.

While the phase shift in Equation 5.5 is sufficient for beam steering with a narrowband signal, a broadband signal has a phase distribution which introduces error if not accounted for. For example, because our radar chirp signal is fairly broadband (500 Mhz), some squinting is experienced with range if we apply only a universal phase shift. Furthermore, by homodyning the signal and taking the FFT prior to beam forming, further complications exist that could introduce

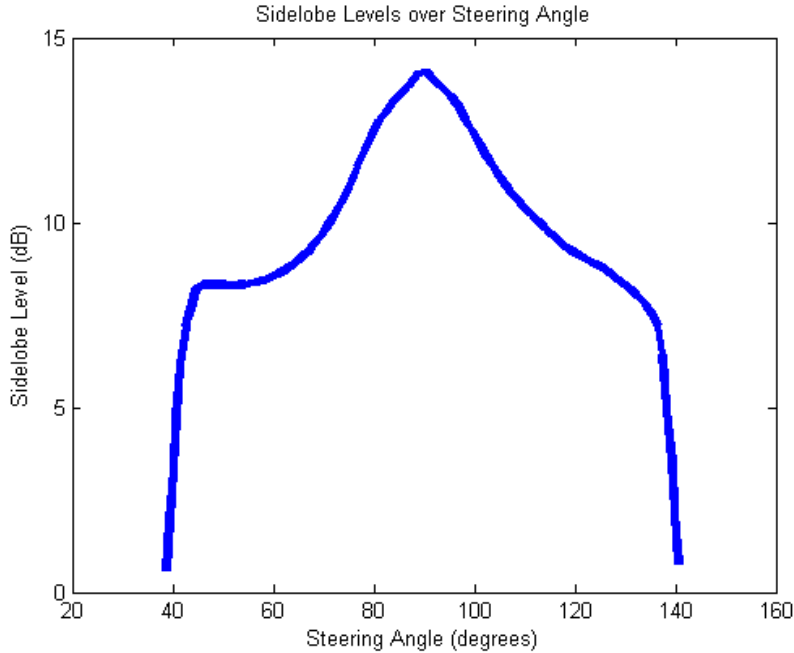


Figure 6.9: The narrow band, simulated side lobe levels for the array, representing the gain of the main lobe minus the largest side lobe’s gain at a given steering angle. They are more than 8 dB over the full 90° steering range. This means that a target at a given range and angle will appear over four times as bright as its image at steering angles where it is in a side lobe.

error in the beam angle. We will explore these two sources of error by examining our signal in Section 6.3.

### 6.3 Broadband Beam Steering

In order to explore the error introduced by a broadband chirp and homodyning, we will begin from the transmit signal modeled as

$$x(t) = \cos(2\pi f_c t + \pi \alpha t^2), \quad (6.6)$$

where  $\alpha = B/T$ . For our radar, the carrier frequency, bandwidth, and chirp period are  $f_c = 10$  GHz,  $B = 0.5$  GHz, and  $T = 1$  ms, respectively.

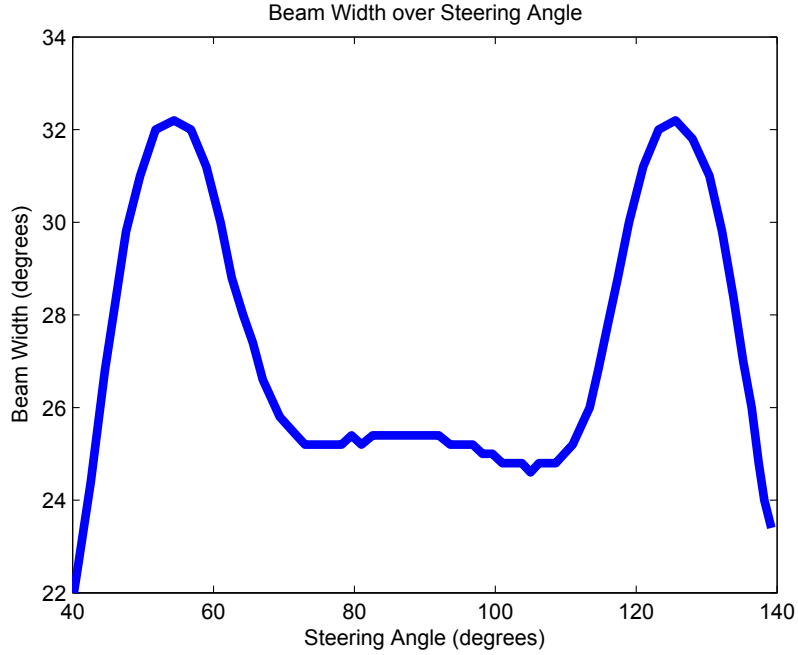


Figure 6.10: The narrow band, simulated 3-dB beam width of the steered beam. This beam width determines how wide targets appear to the radar because as the beam is steered the target remains in the beam over a steering range equal to the beam width. Targets at the edges of the steering range will appear wider than those directly in front of the UAV.

In the ideal case, the received signal has an identical waveform with a time delay of  $\tau_0 = 2r/c_0$  for

$$y(t) = A \cos(2\pi f_c(t - \tau_0 + \pi\alpha(t - \tau_0)^2)) \quad (6.7)$$

$$= A \cos(2\pi f_c(t - \tau_0) + \pi\alpha(t^2 - 2t\tau_0 + \tau_0^2)), \quad (6.8)$$

where  $A$  is a scale factor comprising gain, radar cross section (RCS), and losses. Mixing the two signals produces

$$x(t)y(t) = \cos(u)A \cos(v) \quad (6.9)$$

$$= \frac{A}{2} \cos(u+v) + \cos(u-v), \quad (6.10)$$

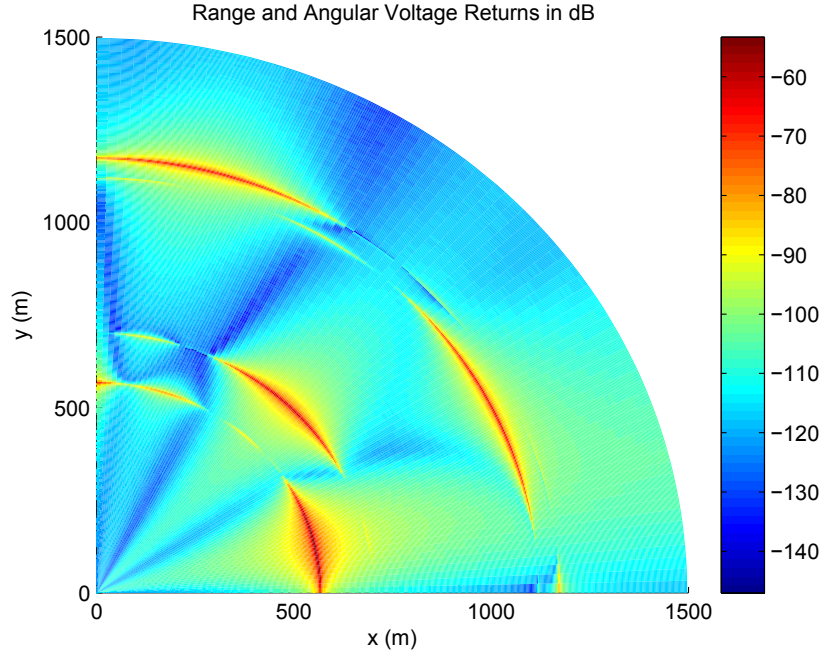


Figure 6.11: The simulated radar image for four targets. Note that each target has weaker ‘ghost images’ where it appeared in the side lobe of the steered beam, especially near the edge of the angular steering range.

where  $u = 2\pi(f_c t + \alpha t^2)$  and  $v = 2\pi f_c(t - \tau_0) + \pi\alpha(t^2 - 2t\tau_0 + \tau_0^2)$ . Since  $u, v > 0$ , we can apply a low-pass filter to remove the  $\cos(u + v)$  term from the equation. This gives us

$$x(t)y(t) = \frac{A}{2} \cos(2\pi f_c \tau_0 + \pi\alpha(2t\tau_0 - \tau_0^2)) \quad (6.11)$$

$$= \frac{A}{2} \cos(2\pi\alpha\tau_0 t + \phi), \quad (6.12)$$

where  $\phi = 2\pi f_c \tau_0 - \pi\alpha\tau_0^2$  is a phase shift factor. This gives a tone associated with the range to the target of  $\Delta f = \alpha\tau_0$ .

Applying this to an array of receive antennas, we get a homodyned signal associated with each antenna,  $i$ , expressed as

$$h_i(t) = \frac{A}{2} \cos(2\pi\alpha\tau_i t + \phi_i), \quad \text{for } i = 0, 1, 2, \dots, N-1, \quad (6.13)$$

where  $N$  is the number of elements,  $d_s$  is the spacing distance between array elements, and  $\theta_a$  is the angle of incidence of the signal from the target. Here,  $\Delta f_i = \alpha \tau_i$  is a factor only of  $\tau_i = \tau_0 + \frac{r_i - r_0}{c_0}$  (where  $r_i = r_0 + i * d_s \cos(\theta_a)$ ) and  $\alpha$ . It is a beat frequency representing the range to the target. The phase terms,  $\phi_i = 2\pi f_c \tau_i - \pi \alpha \tau_i^2$ , represent the time-independent phase at each antenna element.

Because  $d_s$  is negligible compared to the size of a range bin, we can assume  $\Delta f_i = \Delta f_j \forall i, j$  for determining range. However, the differences in phase are key to determining the angle of arrival of the signal. These differences in phase come in four terms within the cosine:

$$\frac{A}{2} \cos(\pi(2\alpha\tau_0 t + 2f_c\tau_0 - \alpha\tau_0^2 + \underbrace{2\alpha(\tau_i - \tau_0)t}_{\phi_a} + \underbrace{2f_c(\tau_i - \tau_0)}_{\phi_b} - \underbrace{\alpha(\tau_i - \tau_0)^2}_{\phi_c} - \underbrace{\alpha\tau_0(\tau_i - \tau_0)}_{\phi_d})). \quad (6.14)$$

To understand the relative scale of these phase-difference terms, we separate them and compute values for our radar chirp parameters:  $B = 5 \times 10^8$  Hz,  $T_c = 1 \times 10^{-3}$  s,  $f_c = 10 \times 10^9$  Hz,  $\tau_i - \tau_0 < id_s/c_0 = i5 \times 10^{-11}$  s,  $\tau_0 < 1.33 \times 10^{-5}$  s (given a maximum range of 2 kilometers,  $r_{max} = 2 \times 10^3$ ), and  $t < T_c$ . In the worst-case scenario,

$$\phi_a^i = 2\pi\alpha(\tau_i - \tau_0)t \quad (6.15)$$

$$< 2\pi B/T_c(id_s/c_0)T_c = i1.57 \times 10^{-1} \quad (6.16)$$

represents a potentially significant phase dispersion over the course of a single chirp.

The phase term  $\phi_b^i$  is limited by

$$\phi_b^i = 2\pi f_c(\tau_i - \tau_0) < \pi i \quad (6.17)$$

in the worst-case scenario. It is the basic phase shift discussed in Section 6.2. It is the primary source of phase difference from element to element and is easily accounted for.

The term  $\phi_c^i$  is introduced by homodyning the received signal and has an upper bound of

$$\phi_c^i = \pi\alpha(\tau_i - \tau_0)^2 \quad (6.18)$$

$$< \pi B/T_c(id_s/c_0)^2 < i^2 3.93 \times 10^{-9} \quad (6.19)$$

in our system. Its magnitude is quadratically related to the physical size of the array, but it is hard to imagine an array used for homodyning radar that is large enough for this term to become significant.

Finally, the  $\phi_d^i$  term, present in beam steering for any broadband signal, is given by

$$\phi_d^i = \pi\alpha\tau_0(\tau_i - \tau_0) < i1.05 \times 10^{-3}. \quad (6.20)$$

In homodyning,  $\phi_d^i$  is a phase term associated with the beat frequency of the mixed down signal. It is directly related to the range to the target by the time delay to the target and back, since it is the difference in frequency of the transmit from the receive chirp that defines the beat frequency.

Having established the relative magnitudes of these phase shifts, we will now discuss them in order from greatest magnitude to least magnitude,  $\phi_b$  in Section 6.3.1,  $\phi_a$  in Section 6.3.2,  $\phi_d$  in Section 6.3.3, and  $\phi_c$  in Section 6.3.4. In each of these sections we will discuss what the phase shift represents, ways to account for the phase shift in beam steering, and the error the phase shift would introduce into our algorithm if not accounted for.

### 6.3.1 Carrier Frequency Phase Shift

We can show that this phase shift,  $\phi_b$ , is equivalent to the phase shift in Equation 6.5 for a narrow band. It is associated with the carrier frequency  $f_c$ , the frequency above which the radar's chirp is modulated. A substitution of terms gives

$$\phi_b^i = 2\pi f_c(\tau_i - \tau_0) \quad (6.21)$$

$$= 2\pi f_c i d_s / c_0 \cos(\theta_a) \quad (6.22)$$

$$= i k d_s \cos(\theta_a). \quad (6.23)$$

It is clear that  $\phi_b$  is the same phase shift formulation  $\Delta\phi$  as seen for a narrowband signal in Equation 6.5. We can account for this phase shift for beam steering as discussed in Section 6.2. This phase term is the classical phase shift used for basic beam steering.

## Implementing the Phase Shift

We implement this phase shift by applying a progressive phase shift to each of the antennas. In our system, the phase shift will be applied to the Fourier transformed signal  $X_i$  from each antenna  $i$  individually to obtain the phase shifted signal  $Y_i$  in the form

$$Y_i(j\omega) = X_i(j\omega)e^{-j\phi_b^i} \quad (6.24)$$

$$= X_i(j\omega)e^{-jkd_s \cos(\theta_a)}. \quad (6.25)$$

This same implementation is used for applying any phase shift to the Fourier domain signal. After all phase shifts have been applied, we sum the  $Y_i$  signals, which add constructively for signals incident from angle  $\theta_a$ .

### 6.3.2 Homodyne Chirp Dispersion

The  $\phi_a$  phase difference term is time dependent on the scale of a single chirp, and this information is lost in the process of the dechirping. Not accounting for it will introduce angular dispersion dependent on angle-of-arrival  $\theta_a$  and the bandwidth  $B$  of the chirp.

The phase dispersion can be given as

$$\phi_a^i = 2\pi\alpha(\tau_i - \tau_0)t, \text{ for } 0 \leq t \leq T_c \quad (6.26)$$

$$= 2\pi B/T_c(id_s \cos(\theta_a)/c_0)t, \text{ for } 0 \leq t \leq T_c. \quad (6.27)$$

This gives a uniform phase distribution over the period of the chirp. The range of this uniform distribution is given by

$$0 \leq \phi_a^i \leq 2\pi Bid_s \cos(\theta_a)/c_0 \quad (6.28)$$

$$0 \leq \phi_a^i \leq i\pi/Q \cos(\theta_a), \quad (6.29)$$

where  $Q = f_c/B$ . The practical implication of this uniform phase dispersion is that the steered beam looks wider by a few degrees and has a reduced gain. While still homodyning, the best we can do is apply a phase shift  $\phi_a$  at the center of the range so the dispersion is uniform and centered

about our intended steering angle. This approach results in a dispersion range dependent on our steering angle  $\theta_a$  and our  $Q$ . In our case

$$\theta_a^{max} = \pi/4 \quad (6.30)$$

$$0 \leq \phi_a^i \leq i\pi 2.5 \times 10^{-2} \sqrt{2}. \quad (6.31)$$

This results in a worst-case phase dispersion range of  $1.11 \times 10^{-1}$  radians, or  $3.6^\circ$  for a four-element array with indexes -1, 0, 1, 2. This corresponds to a beam width increase of  $3.7^\circ$ , over 10%. This reduction in array performance may be enough to motivate a different approach to the sense-and-avoid radar design.

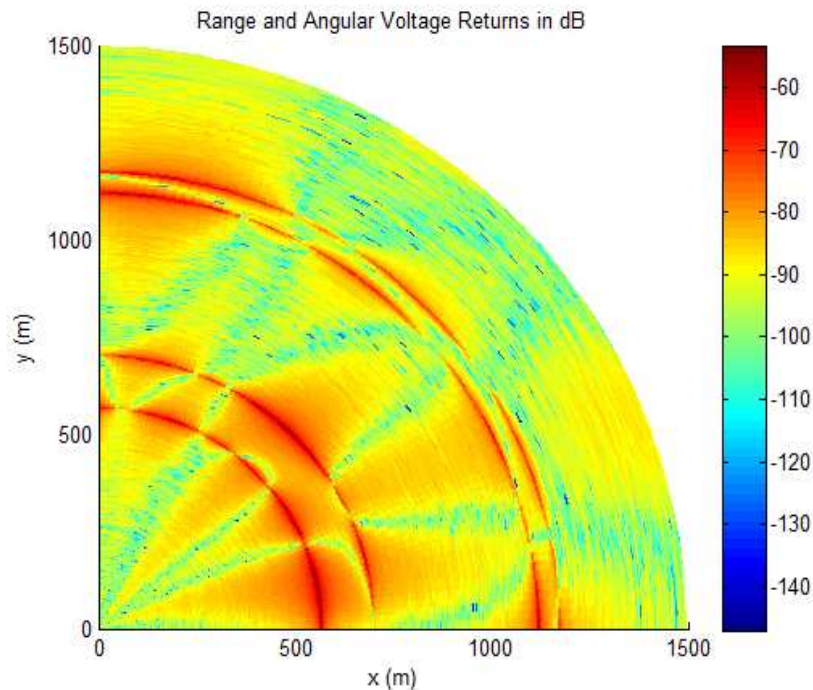


Figure 6.12: This is a radar image like that in Figure 6.11, except that the homodyning dispersion and other broadband effects discussed in Section 6.3 are present in the simulation. The noise level is higher and side lobes are stronger relative to the main lobe. Side lobes also appear to have become more frequent and some targets are indiscernible from their ‘ghost images’ in sidelobes.

## Possible Solutions

This phase dispersion is a result of homodyning, so by using a direct sampling method, it can be prevented or accounted for as long as the processing can be synchronized with the transmit chirp.

### 6.3.3 Beat Frequency Beam Squinting

The phase shift  $\phi_d$  is directly related to the range to the target. Its effect is negligible in our system. While very broadband receive systems (for example, in radio astronomy), must account for this bin frequency in their beam steering, radar systems will not generally experience this squinting.

Though the error is negligible in our application, its significance to other applications means that there is a known solution that we can use to remove the squinting after the FFT. An additional phase shift can simply be applied to each frequency bin independently, corresponding to the additional phase shift experienced at that beat frequency, which corresponds to a range. We obtain this phase shift as

$$\phi_d^i = \pi \alpha \tau_0 (\tau_i - \tau_0) \quad (6.32)$$

$$= \pi B / T_c 2r_0 / c_0 (id_s \cos(\theta_a) / c_0) \quad (6.33)$$

$$= \pi f_b (id_s / c_0 \cos(\theta_a)), \quad (6.34)$$

where  $f_b = B / T_c 2r_0 / c_0$  is the frequency corresponding to each frequency bin. This frequency shift is applied in the same fashion presented in Section 6.3.1. However, in our system, applying this phase shift may not merit the additional processing power and code complexity.

### 6.3.4 Large Array Phase Contribution

This final component of the phase difference between array elements is again the result of homodyning. While it introduces still less beam steering error than the previous component, it can

be easily accounted for in the same way other phase shifts are. The phase shift is given by

$$\phi_c^i = \pi\alpha(\tau_i - \tau_0)^2 \quad (6.35)$$

$$= \pi B/T_c(id_s/c_0\cos(\theta_a))^2. \quad (6.36)$$

While for our application this phase shift is irrelevant, in an array with wider element spacing or a high number of elements, it increases rapidly. A faster chirp rate also affects this phase shift, but only linearly, whereas the physical length of the array has a quadratic impact. This term is negligible for all but the largest of arrays and only exists when homodyning.

#### 6.4 Summary

The 4x1 Vivaldi array element has an antenna pattern ideal for our forward-looking, sense-and-avoid radar. It has a narrow vertical beam and wide horizontal beam, thereby achieving a wide field of view while reducing the impact of clutter on tracking algorithms.

By arraying four of these elements in a 4x4 Vivaldi receive array, we can achieve digital beam steering in the horizontal dimension. This beam steering allows us to derive angle-of-arrival information from the radar return and better avoid collisions. Because we are homodyning our signal, error terms are introduced into the phase. While most of these are negligible, the phase dispersion resulting directly from chirp homodyning cannot be fully removed and results in a wider beam width and lower gain at steering angles far off boresight. This effectively reduces the 3 dB steering range of the 4x4 array from 90° to 80°.

## **CHAPTER 7. CONCLUSION**

In this thesis I have put forward a number of antenna designs well suited for applications in UAS. These include communications antennas and radar antennas.

The circularly polarized antenna presented is small and cheap and, in an array, could be used to transmit or receive high quality CP signals at 20 GHz. In its current configuration, the antenna has very narrow patterns of low axial ratio that change with frequency, but it shows potential for improvement.

My analysis of PCB endfire antenna structures shows that while more expensive substrates can be used to reduce the size of the antenna, the Vivaldi antenna structure seems to have the highest gain and bandwidth. The printed Yagi and SIW horn antennas have a better front-to-back ratio than the Vivaldi, however. The SIW horn has a significantly lower bandwidth than the other structures, but its high gain and very regular pattern are major advantages to many applications.

The monopole over meta-reflector antenna demonstrates the potential in using a simple sub-wavelength grating (SWG) reflector to create a directive pattern. The fact that this meta-reflector has a better aperture efficiency than the metal cone is a compelling argument for the virtue of a planar, focusing reflector using SWG.

The Vivaldi array has a high gain, and when arrayed with other Vivaldi arrays using digital beam forming on the receive side, it is an effective antenna for reducing clutter signals and tracking multiple obstacles for obstacle avoidance. The phase-dispersion term introduced by homodyning cannot be removed and results in a wider beam. This can be avoided by using a direct sampling radar.

### **7.1 Future Work**

Though the circularly polarized antenna shows promise, it needs to be further developed to increase the angular range over which it transmits and receives high quality CP. Continuing

the optimization-based approach to its design, additional degrees of freedom can be added to the optimization. One of these degrees of freedom could be the shape of the patch. Though it is currently constrained to be a square patch with chamfered corners, a kite-shaped patch could be manipulated in various ways during optimization. Similarly, while the current design is constrained to a two-pronged feed, optimizing the locations of additional prongs would increase the domain of optimization and possibly improve the frequency response of the circular polarization.

One aspect of the endfire antennas that I could not compare, but would be useful to compare, is their coupling. This would require developing a model of the printed Yagi and SIW horn antenna structures in order to simulate their coupling characteristics. This is important to know for purposes of arrays of these endfire antennas. It would also be useful to compare these antenna structures using the same substrates for a more meaningful comparison of their performance.

In-application testing is needed for the annular pattern antenna to verify its performance. The intention is for the null at nadir to prevent saturation of amplifiers and so provide more consistent data points for navigation. How significantly this improves performance can only be determined as part of the larger system.

Further testing of the 4x4, 4-channel Vivaldi array in the actual radar system is also required to verify the effectiveness of the beam steering algorithm for detecting and tracking obstacles.

## REFERENCES

- [1] “More about Balloons,” *Scientific American*, vol. 4, no. 26, p. 205, 1849. 1
- [2] Hargrave, “The first air raid - by balloons!” [http://www.ctie.monash.edu/hargrave/rpav\\_home.html](http://www.ctie.monash.edu/hargrave/rpav_home.html), 2014, accessed: Oct. 9, 2014. 1
- [3] J. Mackie, J. Spencer, and K. F. Warnick, “Compact FMCW radar for a UAS sense and avoid system,” in *Antennas and Propagation Society International Symposium (APSURSI)*, Memphis, USA, July 7-13 2014, pp. 1–2. 3, 41
- [4] W. Simon, T. Klein, and O. Litschke, “Small and light 24 GHz multi-channel radar,” in *Antennas and Propagation Society International Symposium (APSURSI)*, Memphis, USA, July 7-13 2014, pp. 1–2. 3
- [5] A. Jam, K. Sarabandi, and M. Vahidpour, “A novel frequency beam-steering antenna array at Y-band,” in *Antennas and Propagation Society International Symposium (APSURSI)*, Memphis, USA, July 7-13 2014, pp. 1–2. 3
- [6] F. Trotta, A. Manna, and L. Scorrano, “A small lightweight wideband printed dipole for UAV applications,” in *Antennas and Propagation Society International Symposium (APSURSI)*, Memphis, USA, July 7-13 2014, pp. 1–2. 3
- [7] Y. Chen and C. Wang, “Electrically small UAV antenna design using characteristic modes,” *Antennas and Propagation, IEEE Transactions on*, vol. 62, no. 2, pp. 535 – 545, 2014. 3
- [8] J. Chalas, K. Sertel, and J. L. Volakis, “NVIS synthesis for electrically small aircraft using characteristic modes,” in *Antennas and Propagation Society International Symposium (APSURSI)*, Memphis, USA, July 7-13 2014, pp. 1–2. 3
- [9] F. J. Drummond and G. H. Huff, “Impact of control surfaces and flight modes for flying-wing UAVs based on an aerodynamically functionalized broadband antenna,” in *Antennas and Propagation Society International Symposium (APSURSI)*, Memphis, USA, July 7-13 2014, pp. 1–2. 3
- [10] A. Madanayake, L. Belostotskiy, C. Wijenayake, L. Brutony, and V. Devabhaktuniz, “Analog 2-D IIR beam filters for EARS in UAS ecosystems,” in *Antennas and Propagation Society International Symposium (APSURSI)*, Memphis, USA, July 7-13 2014, pp. 1–2. 3
- [11] M. Martinez-Vazquez and S. Weitz, “Low-cost UAS ground station antenna for high quality video streaming at 5.8 GHz,” in *Antennas and Propagation Society International Symposium (APSURSI)*, Memphis, USA, July 7-13 2014, pp. 1–2. 3
- [12] W. M. Dorsey and A. I. Zaghoul, “Dual-band, dual-circularly polarised antenna element,” *Microwaves, Antennas & Propagation, IET*, vol. 7, no. 4, 2013. 4

- [13] R. Jefferson and D. Smith, "Dual circular polarised microstrip antenna design for a passive microwave transponder," in *Antennas and Propagation, 1991. ICAP 91., Seventh International Conference on (IEE)*. IET, 1991, pp. 141–143. 4
- [14] M. R. Morin, "Design and analysis of receiver systems in satellite communications and UAV navigation radar," Master's thesis, Brigham Young University, 2014. 4
- [15] R. van Dijk, E. van der Houwen, and A. Maas, "Multi-mode FMCW radar array with independent digital beam steering for transmit and receive," in *Radar Conference, 2008. EuRAD 2008. European*. IEEE, 2008, pp. 412–415. 5
- [16] A. Huizing, M. Otten, W. van Rossum, R. Van Dijk, A. Maas, E. Van der Houwen, and R. Bolt, "Compact scalable multifunction RF payload for UAVs with FMCW radar and ESM functionality," in *Radar Conference-Surveillance for a Safer World, 2009. RADAR. International*. IEEE, 2009, pp. 1–6. 5
- [17] D. Platt, L. Pettersson, D. Jakonis, M. Salter, and J. Haglund, "Integrated 79 GHz UWB automotive radar front-end based on Hi-Mission MCM-D silicon platform," *International Journal of Microwave and Wireless Technologies*, vol. 2, no. 3-4, pp. 325–332, 2010. 5
- [18] IEEE, "IEEE standard definitions of terms for antennas." *IEEE Std 145-1993*, 1993. 7
- [19] ———, "IEEE standard definitions of terms for radio wave propagation," *IEEE Std 211-1997*, 1998. 7
- [20] D. M. Pozar, *Microwave Engineering, Third Edition*. John Wiley & Sons, Inc., 2012. 7
- [21] F. T. Ulaby, E. Michielssen, and U. Ravaioli, *Fundamentals of Applied Electromagnetics, 6th edition*. Pearson Education, Inc., 2010. 7
- [22] T. Manabe, K. Sato, H. Masuzawa, K. Taira, T. Ihara, Y. Kasashima, and K. Yamaki, "Polarization dependence of multipath propagation and high-speed transmission characteristics of indoor millimeter-wave channel at 60 GHz," *Vehicular Technology, IEEE Transactions on*, vol. 44, no. 2, pp. 268–274, 1995. 13
- [23] M. Khan, Z. Yang, and K. F. Warnick, "Dual circular polarized high efficiency antenna for Ku band satellite communication," *Antennas and Propagation, IEEE Transactions on*, 2014. 13
- [24] Z. Yang and K. F. Warnick, "Effect of mutual coupling on the sensitivity of dual polarized receivers in satellite communications," in *Antennas and Propagation Society International Symposium (APSURSI)*, Memphis, USA, July 7-13 2014, pp. 1–2. 17
- [25] P. Hall, J. Dahele, and J. James, "Design principles of sequentially fed, wide bandwidth, circularly polarised microstrip antennas," in *IEE Proceedings H (Microwaves, Antennas and Propagation)*, vol. 136. IET, 1989, pp. 381–389. 21
- [26] U. R. Kraft, "An experimental study on  $2 \times 2$  sequential-rotation arrays with circularly polarized microstrip radiators," *Antennas and Propagation, IEEE Transactions on*, vol. 45, no. 10, pp. 1459–1466, 1997. 21

- [27] S. S. Yang, K. Lee, A. A. Kishk, and K. M. LUK, "Design and study of wideband single feed circularly polarized microstrip antennas," *Progress In Electromagnetics Research*, 2008. 21
- [28] O. Kim and K. Chen, "Flush-mounted, scanning end-fire antenna with corrugated surface wave structures," *Antennas and Propagation Society International Symposium*, vol. 11, pp. 164–167, 1973. 23
- [29] M. S. Sharawi, D. N. Aloii, and O. A. Rawashdeh, "Design and implementation of embedded printed antenna arrays in small UAV wing structures," *Antennas and Propagation, IEEE Transactions on*, vol. 58, no. 8, pp. 2531–2538, 2010. 25
- [30] H. K. Kan, R. B. Waterhouse, A. M. Abbosh, and M. E. Bialkowski, "Simple broadband planar CPW-fed quasi-Yagi antenna." *Antennas and Wireless Propagation Letters*, no. 6, pp. 18–20, 2007. 29
- [31] M. Esquiús-Morote, B. Fuchs, J. Zurcher, and J. R. Mosig, "Novel thin and compact H-plane SIW horn antenna," *Antennas and Propagation, IEEE Transactions on*, vol. 61, no. 6, pp. 2911–2920, 2013. 29
- [32] P. deFranco, J. Mackie, and K. F. Warnick, "Electromagnetic orientation using MIMO channel sounding in a GPS-denied environment," in *USNC-URSI National Radio Science Meeting*, Orlando, FL, July 7-13 2013. 33, 38
- [33] S. S. Wang, R. Magnusson, J. S. Bagby, and M. G. Moharam, "Guided-mode resonances in planar dielectric-layer diffraction gratings," *Journal of the Optical Society of America A*, vol. 7, no. 8, pp. 1470–1474, 1990. 35
- [34] D. Fattal, J. Li, Z. Peng, M. Fiorentino, and R. G. Beausoleil, "Flat dielectric grating reflectors with focusing abilities," *Natural Photonics*, vol. 4, no. 7, pp. 466–470, 2010. 35
- [35] R. Ross, "Radar cross section of rectangular flat plates as a function of aspect angle," *Antennas and Propagation, IEEE Transactions on*, vol. 14, no. 3, pp. 329–335, 1966. 36
- [36] P. deFranco, J. Mackie, M. Morin, and K. F. Warnick, "Bio-inspired electromagnetic orientation for UAVs in a GPS-denied environment using MIMO channel sounding," *Antennas and Propagation, IEEE Transactions on*, vol. 62, no. 10, pp. 5250–5259, 2014. 38